Two Decades of Pacific Anthropogenic Carbon Storage and Ocean Acidification Along GO-SHIP Sections P16 and P02

Carter, B.R.[1,2], Feely, R.A.[2], Mecking, S.[3], Cross, J. N.[2], Macdonald, A. M.[4], Siedlecki, S. A.[1], Talley, L. D.[5], Sabine, C. L.[2], Millero, F. J.[6], Swift, J. H.[5], Dickson, A. G.[5], and Rodgers, K. B.[7]

Deleted: and

[1]Joint Institute for the Study of the Atmosphere and Ocean, University of Washington, 3737 Brooklyn Avenue NE, Seattle, WA, 98105, USA

[2]NOAA Pacific Marine Environmental Laboratory, 7600 Sand Point Way, Seattle, WA, USA

[3]Applied Physics Laboratory, University of Washington, Seattle, WA, USA 98105;

[4]Woods Hole Oceanographic Institution, Woods Hole, MA, USA 02543

[5]Scripps Institution of Oceanography, University of California, San Diego, La Jolla, CA, USA

[6]Rosenstiel School of Marine and Atmospheric Science, University of Miami, 4600 Rickenbacker Causeway, Miami, FL, USA, 33149

[7] Atmospheric and Oceanic Sciences Program, Princeton University, Princeton, New Jersey, USA

Abstract

A modified version of the extended multiple linear regression (eMLR) method is used to estimate anthropogenic carbon concentration (C_{anth}) changes along the Pacific P02 and P16 hydrographic sections over the past two decades. P02 is a zonal section crossing the North Pacific at 30°N and P16 is a meridional section crossing the North and South Pacific at ~150°W. The eMLR modifications allow the uncertainties associated with choices of regression parameters to be both resolved and reduced. C_{anth} is found to have increased throughout the water column from the surface to ~1000 m depth along both lines in both decades. Mean column C_{anth} inventory increased consistently during the earlier (1990s-2000s) and recent (2000s-2010s) decades along P02, at rates of 0.53±0.11 and 0.46±0.11 mol C m^{-2} a^{-1}, respectively. By contrast, C_{anth} storage accelerated from 0.29±0.10 to 0.45±0.11 mol C m^{-2} a^{-1} along P16. Shifts in water mass distributions are ruled out as a potential cause of this increase, which is instead attributed to recent increases in the ventilation of the South Pacific Subtropical Cell. Decadal changes along P16 are extrapolated across the gyre to estimate a Pacific Basin average storage between 60°S and 60°N of 6.1±1.5 PgC $decade^{-1}$ in the earlier decade and 8.8±2.2 PgC $decade^{-1}$ in the recent decade. This storage estimate is large despite the shallow Pacific C_{anth} penetration due to the large volume of the Pacific Ocean. By 2014, C_{anth} storage had changed Pacific surface seawater pH by -0.08 to -0.14 and aragonite saturation state by -0.57 to -0.82.

Deleted: ¶

Deleted: Both sections have been measured at least three times since 1990.

Deleted: substantial

Deleted: 12

Deleted: 12

1. Introduction

Since the beginning of the Industrial Era, the global ocean has absorbed approximately 28% of the anthropogenic carbon dioxide (C_{anth}) emissions released into the atmosphere from fossil fuel burning, land use changes, and cement production [*Canadell et al.*, 2007; *Le Quéré et al.*, 2015]. As of 1994, ~38% of this oceanic C_{anth} resided in the Pacific [*Sabine et al.*, 2002, 2004]. Ocean CO_2 uptake is significant for Earth's climate and ecosystems for several reasons. Atmospheric CO_2 traps heat in the Earth system while marine CO_2 does not, so ocean storage has slowed anthropogenic global warming and warming-induced intensification of the hydrological cycle [*Durack et al.,* 2012]. Ocean CO_2 uptake also reduces seawater pH and carbonate ion concentrations [CO_3^{2-}]. This ocean acidification (OA) is thought likely to have far reaching impacts on ocean ecosystems, particularly on organisms that utilize CO_3^{2-} to form their shells and hard parts [*Doney et al.*, 2009; *Pfister et al.*, 2014; *Gattuso et al.*, 2015; *Gattuso and Feely*, 2016]. Consequently, monitoring carbon and anthropogenic carbon concentrations in the Pacific and the other major ocean basins is a critical task for Earth scientists.

Sabine et al. [2004] estimated global ocean C_{anth} distributions from the 1990s World Ocean Circulation Experiment (WOCE) measurements. Their approach was to subtract estimates of natural carbon concentrations, meaning the carbon that would be expected in the absence of anthropogenic CO_2 emissions, from total dissolved inorganic carbon concentrations (C_T). Scientists have more recently used time-histories of contact between seawater and the atmosphere inferred from other tracer measurements (e.g. through the transit time distribution and maximum entropy methods of *Waugh et al.* [2006] and *Khatiwala et al.* [2009]). These methods provide C_{anth} estimates from individual synoptic surveys, but the methods rely on uncertain assumptions regarding the consistency of water mass ventilation pathways or the shapes of water mass age distributions. In recent decades, the Repeat Hydrography program, a contribution to the U.S. Climate Variability (CLIVAR) program, and the more recent

Deleted:

Moved down [1]: Consequently, recording repeated observations of carbon concentrations in the major ocean basins is a critical task for Earth scientists. As of 1994, ~38% of oceanic C_{anth} resided in the Pacific [*Sabine et al.*, 2002, 2004].

Deleted: :

Deleted: the associated

Moved (insertion) [1]

Deleted: recording repeated observations of

Deleted: As of 1994, ~38% of oceanic C_{anth} resided in the Pacific [*Sabine et al.*, 2002, 2004].

Deleted: subsequent years

international Global Ocean Ship-based Hydrographic Investigations Program (GO-SHIP), repeated a subset of the measurements made along the WOCE hydrographic lines on decadal intervals. These repeated hydrographic transects provide valuable independent information as they allow direct estimation of decadal changes in carbon inventories without relying on the assumptions used by other methods.

Deleted: same

Deleted: , providing valuable independent information

Decadal changes in C_T cannot be solely attributed to anthropogenic carbon uptake due to large natural variability in ocean C_T. *Wallace* [1995] proposed a multiple linear regression (MLR) approach to address the part of these C_T fluctuations resulting from natural variability. This method and the more-commonly used extended MLR (eMLR) [*Friis et al.*, 2005] variant, which is described in greater detail in the methods section, parameterize the influences of natural variability using regressions of C_T against other measured properties. The regressions from one occupation are combined with the measurements from another occupation to estimate the C_T distribution expected if natural variability had been identical in both cases. Differences between measured and expected C_T distributions are then attributed to C_{anth} concentration changes. The eMLR method has been used extensively to quantify decadal ocean C_{anth} changes [e.g. *Sabine et al.*, 2008; *Wanninkhof et al.*, 2010; *Williams et al.*, 2015; *Chu et al.*, 2016; *Woosley et al.*, 2016]. The method has been tested in biogeochemical ocean circulation models with known C_{anth} distributions and shown to be capable of reproducing known modeled regionally averaged anthropogenic carbon inventory changes to within 20% when used judiciously [*Levine et al.*, 2008; *Goodkin et al.*, 2011; *Plancherel et al.*, 2013]. However, eMLR estimate uncertainties are larger at specific locations due in large part to semi-arbitrary decisions concerning the particular parameters to include in the regressions [*Plancherel et al.*, 2013]. In this study, we use the

Deleted: the

Deleted: of which

eMLR approach to estimate decadal C_{anth} storage along the Pacific P16 and P02 sections (Fig. 1) between the early 1990s and 2000s (WOCE to CLIVAR) and between the 2000s and the modern decade (CLIVAR to GOSHIP). We therefore repeat and extend some of the work of *Sabine et al.* [2008], who also considered Pacific C_{anth} accumulation between the 1990s and 2000s along the P02 and P16 sections. Several novel modifications to the method are used (Section 2.2) to reduce the impact of decisions required for eMLR on the estimated C_{anth} values.

Deleted: , also

2. Methods

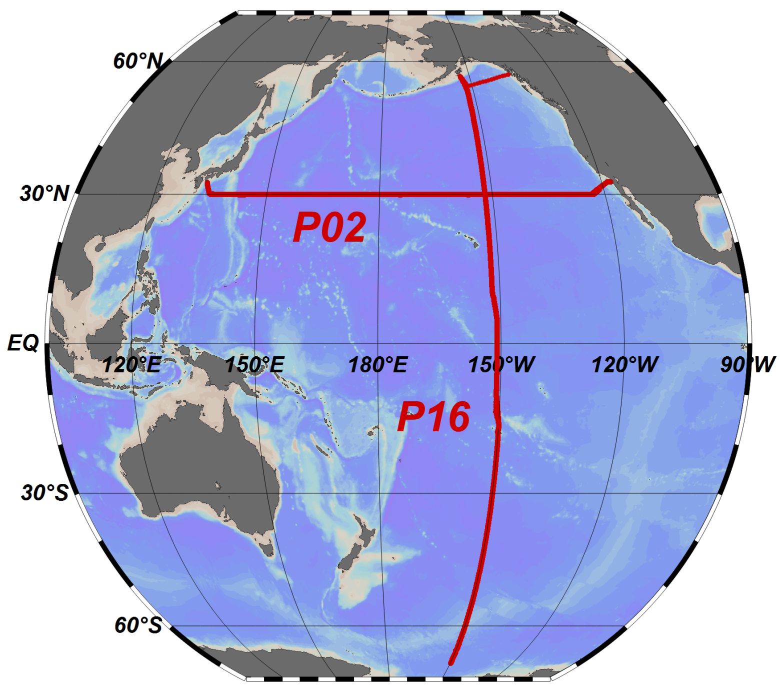

Figure 1. A map of the P02 and P16 sections in the Pacific.

2.1 Data used

Deleted: ¶

Samples were collected along P02 (~30°N) and P16 (~150°W) (Fig. 1) on 16 cruise legs over three decades. Cruise stations were typically separated by 30 nautical miles along the lines and up to 24-36 samples were measured from the ocean surface to the ocean bottom per station. C_T was measured on these samples, allowing us to estimate C_{anth} storage for the ~20 years spanning these sets of measurements. The P02 and P16 transects are chosen because they each have 3 completed occupations. We refer to the six 1990s WOCE era cruise legs as "early" cruises, the five 2000s CLIVAR era cruise legs as "middle" cruises, the five GO-SHIP era 2010s cruise legs as "recent" cruises (cruise Expocodes are provided in Table 1), and the decades spanning these re-occupations as the "earlier" and "recent" decades.

Measurements of temperature (T), salinity (S), oxygen concentration (O_2), total nitrate and nitrite concentration (N), and total silicate concentration (Si) are used in this analysis in addition to C_T. Total seawater titration alkalinity (A_T) is used as a second carbonate system constraint to calculate pCO_2 in the mixed layer. We do not include A_T as a regression parameter due to relatively large adjustments required for deep data consistency. Initial experimentation that did include A_T returned qualitatively similar results but with increased estimate noise. Phosphate concentrations are similarly not used in the regressions because there are large deep-water phosphate changes along P02 between WOCE and CLIVAR, possibly indicating measurement offsets between cruises. Also, since phosphate and N have similar distributions, including phosphate with N adds little independent information to the regressions and brings along the risk of over fitting C_T.

Several steps were taken to prepare the data sets for analysis. First, data flagged in the datasets as questionable or bad are omitted, along with fewer than 10 (out of ~33,000 total property measurements) apparent C_T outlier measurements that appear as 'bulls-eyes' in contour plots. Second, as Pacific Ocean properties are not expected to experience strong changes between 3000 and 4000 m depth (i.e. in Pacific Deep Water) on decadal timescales, adjustments (Table 1) are applied to the later dataset in each comparison to counter any differences observed at these depths. While we believe the adjustments applied are appropriate, we account for the possibility that the adjustments are countering real shifts in water mass properties in our error assessment (Appendix A). For T, S, and O_2, adjustments are applied by subtracting the mean property change over this depth range from all later occupation data. For N, Si, C_T, and A_T the later occupations are divided by the ratio of the mean deep values in the later occupations to the mean values in the earlier occupations. The choice between fixed offsets and multiplicative adjustments was made on a property-by-property basis in light of the kinds of errors that are likely to arise during the measurement analyses. A fixed offset was used when uncertain.

Field Code Changed

Table 1. Cruise Expocodes, years, and adjustments applied to the later dataset in each comparison. All cruise data were acquired from the CLIVAR and Carbon Hydrographic Data Office (CCHDO) data portal.

Expocode	Section	Year	T	S	O_2	N	Si	C_T	A_T
			Offset adjustments [°C]		[µmol kg^{-1}]	*Multiplier adjustments*			
316N138_9*	P16S	1992	-	-	-	-	-	-	-
31WTTUNES_2* 31WTTUNES_3*	P16C	1991	-	-	-	-	-	-	-
31DSCGC91_1*	P16N	1992	-	-	-	-	-	-	-
49K6KY9401_1	P02E	1994	-	-	-	-	-	-	-
49K6KY9401_1	P02W	1994	-	-	-	-	-	-	-
33RR200501	P16S	2005	0.071	0.001	-0.8	0.9948	0.9921	1.0003	0.9985

Formatted Table

325020060213	P16C	2006	-0.068	0.003	-1.6	1.0086	0.9869	1.0001	1.0003
325020060213	P16N	2006	0.009	0.006	-2.8	0.9969	0.9810	1.0001	1.0008
318M200406	P02E	2004	0.054	-0.013	-1.0	1.0089	0.9892	0.9993	1.0043
318M200406	P02W	2004	0.056	-0.024	-1.9	1.0220	0.9888	0.9988	1.0057
320620140320	P16S	2014	0.065	-0.003	-0.3	1.0008	0.9964	1.0000	1.0003
33RO20150410	P16C	2015	0.065	-0.003	-1.7	0.9888	0.9874	0.9996	0.9988
33RO20150525	P16N	2015	0.007	0.002	-1.1	1.0059	0.9890	1.0006	0.9988
318M20130321	P02E	2013	-0.083	-0.006	-0.7	0.9999	1.0064	1.0005	0.9994
318M20130321	P02W	2013	0.006	0.002	-0.3	0.9954	1.0020	1.0003	0.9982

*denotes the cruises where data were extracted data from the GLODAPv1.1 data product of [*Key et al.*, 2004]. This data product calculated A_T from diverse carbonate system parameters when unmeasured.

Potential temperature (θ), potential density (σ_θ), and apparent oxygen utilization (AOU, equivalent to the oxygen deficit relative to atmospheric equilibrium) were calculated using the seawater routines for MATLAB [*Morgan and Pender*, 2006]. Neutral density (γ^N) was calculated using the routines from *Jackett and McDougall* [1997].

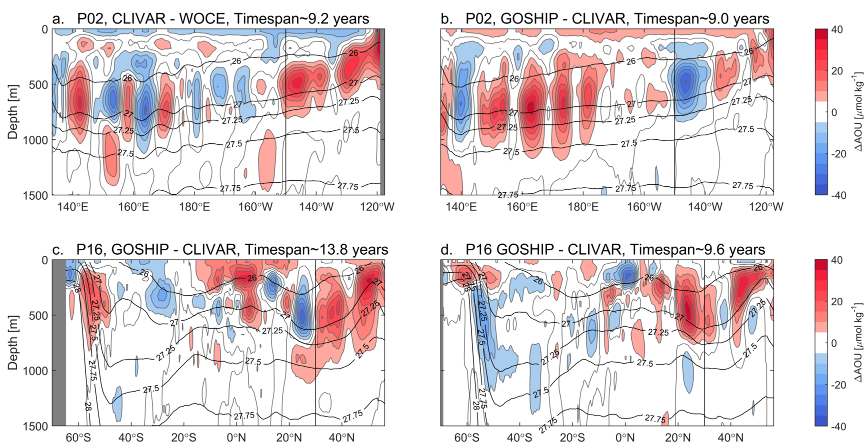

Figure 2. Sections of direct Pacific C_T changes. Sections are **a.** P02 (east-west at ~30°N) in

the earlier decade, **b.** P02 in the recent decade, **c.** P16 (north-south at ~150°W) in the earlier decade, and **d.** P16 in the recent decade. Vertical black lines indicate crossovers between the two sections and curved black lines indicate surfaces of constant γ^N

Deleted: .

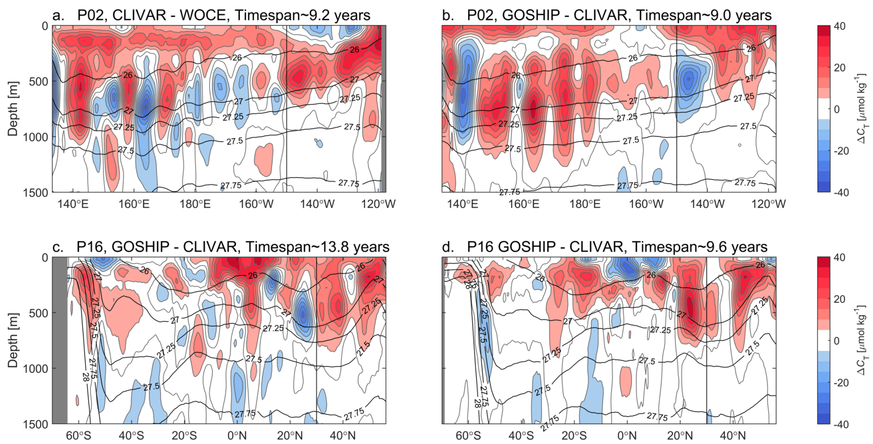

Figure 3. Sections of direct Pacific AOU changes. Sections are **a.** P02 (east-west at ~30°N) in the earlier decade, **b.** P02 in the recent decade, **c.** P16 (north-south at ~150°W) in the earlier decade, and **d.** P16 in the recent decade. Vertical black lines indicate crossovers between the two sections and curved black lines indicate surfaces of constant γ^N

Deleted: .

2.2 Estimating decadal C_{anth} change

Before C_{anth} can be estimated, the impacts of natural variability need to be removed from changes in C_T. These modes of variability include shifts in the locations of water masses on sub-decadal timescales and variability in biogeochemical cycling patterns. The impacts of these modes of variability and ongoing C_{anth} uptake can be seen in large and spatially-variable decadal

C_T (Fig. 2) and AOU (Fig. 3) changes along P02 and P16. We use the eMLR approach to remove the impacts of variability from these measurement change distributions.

The eMLR approach assumes that the natural processes changing C_T also change other measurable seawater properties that are unaffected by C_{anth} uptake. For instance, shifts in water mass locations affect most measured properties, and variability in biogeochemical cycling affects *N*, *Si*, and AOU distributions as well as C_T. The first step in the eMLR approach involves creating empirical linear functions "*f*" from the other measured (e.g. *S*, *N*, *Si*) and derived (e.g. θ, AOU) properties "*P*" to capture the effect of natural variability on C_T (Equation 1):

$$f(P) = C_T \quad (1)$$

Then the function from each decade is applied to the same set of measurements to yield estimates of what the measured C_T would have been had the modes of natural variability acted identically during both occupations. The differences between these estimates are then the portions of C_T changes that are not accounted for by natural variability, which are therefore attributed to C_{anth} uptake (Equation 2). For the earlier decade, this is expressed as:

$$C_{anth} = f_2(P_2) - f_1(P_2) \quad (2)$$

In these equations the subscripts indicate the decades the terms are specific to, with 1 and 2 being the early and middle decades, respectively. The recent decade is later denoted with a 3.

Deleted: 1 and 2

Deleted: terms

Deleted: that are specific to the earlier and more recent decades, respectively.

Goodkin et al. [2011] warn eMLR users that circulation changes will render the empirical relationships determined for an earlier decade unsuitable for reproducing variability in a later decade when reoccupations are separated by 30 years or more, and *Plancherel et al.* [2013] show bias can be introduced when the sampling network is inconsistent between reoccupations.

However, we only consider overlapping portions of sections with maximum reoccupation intervals of 15 years, so neither of these cautions applies to our work.

We use several modifications to the eMLR approach to isolate C_{anth} storage changes from natural C_T variability. Modifications are listed here and details follow. Assertions about the efficacy of these modifications are based on tests detailed in Appendix B:

1. As done by *Friis et al.* [2005], we compare C_T estimates from regressions to one another (Equation 2) rather than directly to the measurements (i.e. we use eMLR, not MLR), thereby cancelling a portion of the C_T fit error.

   Deleted: .

   Formatted: Font: Italic

   Formatted: Subscript

2. As done by *Sabine et al.* [2008], we include an adjustment based on AOU changes to account for potential additional changes in biogeochemical C_T cycling that are not resolved by the eMLR regressions. We find this adjustment decreases mean estimate error and r.m.s. error by ~7-15%.
3. As done by *Velo et al.* [2013] for A_T regressions, we use "robust" multiple linear regression. Robust regression minimizes the impact of outliers on our regressions by iteratively re-estimating regression coefficients after assigning smaller weights to measurements with larger residuals, thereby excluding outliers. We use the "robustfit" MATLAB robust regression routine with a bisquare outlier test and the recommended default turning constant, meaning data with residuals in excess of 4.685 times the standard residuals are given no weight.

   Deleted: , which includes an iterative outlier exclusion step prior to regression

4. Like *Velo et al.* [2013] and *Carter et al.* [2016], we use a moving window in depth, γ^N, and latitude or longitude to select data for each regression. This moving window removes the need to make arbitrary decisions regarding which depth or density intervals

to use for each regression, and reduces the number of independent variables required to capture the modes of variability along hydrographic sections bisecting many heterogeneous water masses. Omitting the moving window doubles mean errors, though most error increase occurs when omitting the moving window in depth/density, and many previous studies have included multiple regressions for various depth ranges. Omitting the horizontal component of the moving window only improves mean error by ~10%. Neither window has a strong impact on r.m.s. error. The primary advantage the moving window offers is eliminating the need for choices regarding how to partition the water column vertically.

5. Finally, we use 16 combinations (Table 2) of our 5 regression seawater properties (θ, *S*, AOU, *Si*, and *N*) for our regressions and use the mean C_{anth} estimate returned by these varied regressions as our final C_{anth} estimates. *Plancherel et al.* [2013] tested various approaches for reconstructing known simulated C_{anth} distributions and showed that the choice of which properties to include in a regression can have a substantial impact on the C_{anth} estimates returned. Their mean estimate was also somewhat better than the estimate from the best AIC approach, which scrupulously chose the regression parameter combination with the best fit relative to the number of degrees of freedom for several depth intervals. We find this adjustment decreases our mean estimate errors by ~30-40% and r.m.s. errors by ~60-80%.

Deleted: many

We are unaware of steps 3 through 5 being used for eMLR ΔC_{anth} estimates before. We refer to our approach as an "ensemble eMLR" because of step 5.

The first step of the ensemble eMLR method is to select "local" data for each of our 33,000+ regression locations by applying moving windows around each data point (one for each measured location in each dataset). Local data are data remaining after excluding all measurements:

1. within the mixed layer (more below),
2. more than 15° of latitude or longitude away,
3. found on a different hydrographic line than the location (i.e. along P02 vs. P16), and
4. that are both more than 200 m deeper or shallower and either 0.1 kg m^{-3} γ^N denser or less dense than the density of the seawater for which regression constants are being determined.

Requirement 4 is designed to have the local data window rely on γ^N, but it also includes a depth threshold to ensure the inclusion of enough measurements to constrain a regression within regions of large vertical density gradients.

Next, the regression coefficients are estimated for C_T. The general form of the equation fit to data is:

$$C_T = \alpha_1^1 + i^\theta \alpha_1^\theta \theta + i^S \alpha_1^S S + i^N \alpha_1^N N + i^{Si} \alpha_1^{Si} Si + i^{AOU} \alpha_1^{AOU} AOU \qquad (3)$$

In Equations 3 and 4, the α values are the regression coefficients. Superscripts link coefficients to their associated predictors, and subscripts refer to occupations (as before). The i terms are either 1's or 0's depending on whether the specific regressions contain each of the 5 properties (see Table 2). Regression coefficients are similarly estimated for AOU for the 5 regressions that omit AOU as a predictor variable:

$$AOU = \beta_1^1 + i^\theta \beta_1^\theta \theta + i^S \beta_1^S S + i^N \beta_1^N N + i^{Si} \beta_1^{Si} Si \qquad (4)$$

Deleted: both AOU and

Deleted: Example regressions using θ, S, and N are:

Deleted:

$$AOU = c_{AOU}^1 + i_\theta c_{AOU}^\theta \theta + i_S c_{AOU}^S S + i_N c_{AOU}^N N + i_{Si} c_{AOU}^{Si} S$$

(4)

Field Code Changed

Deleted: lowercase c

Deleted: and subscripts

Deleted: and independent variables

Deleted: , respectively

Deleted: Regressions with 16 combinations of 3 to

Field Code Changed

β regression coefficients are estimated at every location for which there are C_T measurements in the early, middle, and recent datasets. These regressions implicitly include latitude/longitude and depth as regression coefficients by virtue of allowing the fits to change in space. It is possible to obtain smaller regression residuals using fits with more regression parameters. However, the strength of regression fits has been shown to be a poor indicator of eMLR skill and including more regression parameters increases the risk of over fitting the signal. We therefore consider estimates from each of these 16 regressions to be equally likely. For discussion purposes only, a 17th regression is performed using only θ and S.

Table 2. Properties used in each of the 16 regressions for C_T. A "1" indicates the property is used and a "0" indicates it is not. AOU is regressed only for the 5 regressions with i_{AOU} of 0.

Reg. #	i_θ	i_S	i_{AOU}	i_N	i_{Si}
1	1	1	1	0	0
2	1	1	0	1	0
3	1	1	0	0	1
4	1	0	1	1	0
5	1	0	1	0	1
6	1	0	0	1	1
7	0	1	1	1	0
8	0	1	1	0	1
9	0	1	0	1	1
10	0	0	1	1	1
11	1	1	1	1	0
12	1	1	1	0	1
13	1	1	0	1	1
14	1	0	1	1	1
15	0	1	1	1	1
16	1	1	1	1	1

The next step in the process is to grid the regression coefficients from the paired datasets onto a regular 2D depth-longitude grid. Properties are gridded vertically onto every 50 m increment between 25 m and 5475 m depth using the cubic Hermite piecewise polynomial linear interpolation scheme described by *Carter et al.* [2014] (Supplementary Materials section SA). Seawater properties and regression coefficients are then linearly interpolated onto every quarter degree of longitude and latitude along the two sections. All further analysis is carried out using these gridded values. However, for figure clarity, data are smoothed using a ±1° latitude or longitude averaging window centered on each grid point before plotting sections.

The residual portions of AOU and C_T water-mass changes that are not captured by the regressions (r_{AOU} and r_C) are estimated at each grid location for each regression by differencing the interpolated regression coefficients according to equations (5) and (6) and multiplying by the property distributions:

$$\begin{aligned} r_C = {} & (\alpha_2^1 - \alpha_1^1) + i_\theta(\alpha_2^\theta - \alpha_1^\theta)\theta + i_S(\alpha_2^S - \alpha_1^S)S + i_{\mathrm{AOU}}(\alpha_2^{\mathrm{AOU}} - \alpha_1^{\mathrm{AOU}})\mathrm{AOU} + \\ & + i_N(\alpha_2^N - \alpha_1^N)N + i_{Si}(\alpha_2^{Si} - \alpha_1^{Si})Si \end{aligned} \quad (5)$$

$$\begin{aligned} r_{\mathrm{AOU}} = {} & (\beta_2^1 - \beta_1^1) + i_\theta(\beta_2^\theta - \beta_1^\theta)\theta + i_S(\beta_2^S - \beta_1^S)S + i_{\mathrm{AOU}}(\beta_2^{\mathrm{AOU}} - \beta_1^{\mathrm{AOU}})\mathrm{AOU} + \\ & + i_N(\beta_2^N - \beta_1^N)N + i_{Si}(\beta_2^{Si} - \beta_1^{Si})Si \end{aligned} \quad (6)$$

Equation (6) is only applied to the 5 regressions lacking AOU as a predictor variable (Table 2). Except when otherwise specified, the property values used to estimate these changes are from the later occupation of each pair. We caution that r_{AOU} estimates are not equivalent to AOU changes at a location (ΔAOU), as a portion of ΔAOU will correlate with the regression parameters and be removed by Equation (6) (see also Section 3.1).

Deleted:

Field Code Changed

Deleted: $r_{\mathrm{AOU}} = (C_{\mathrm{AOU}}^1 - c_{\mathrm{AOU}}^1) + i_\theta(C_{\mathrm{AOU}}^\theta - c_{\mathrm{AOU}}^\theta)\theta + i_S(C \ldots$ $+ i_N(C_{\mathrm{AOU}}^N - c_{\mathrm{AOU}}^N)N + i_{Si}(C_{\mathrm{AOU}}^{Si} - c_{\mathrm{AOU}}^{Si})S \ldots$

Deleted: In Equations 5 and 6, lowercase constants are from the earlier occupations and capitalized constants are from the recent occupations

Deleted: θ, S, and N

Formatted: Font: Not Italic

Formatted: Font: Not Italic

Formatted: Font: Not Italic

Formatted: Font: Not Italic

Field Code Changed

Deleted: R_{AOU}

Deleted: n unknown

Deleted: the

Deleted: change

Following *Sabine et al.* [2008], the portion of r_C attributable to changes in net biological remineralization (ΔC_{bio}) was estimated as the product of ΔAOU and a remineralization ratio [*Anderson and Sarmiento*, 1994]:

$$\Delta C_{bio} = r_{AOU}\,\frac{117\ \mu mol\ C}{170\ \mu mol\ O_2} \tag{7}$$

For the 5 regressions without AOU, this term is subtracted from r_C to adjust for redistribution of C_T from remineralized organic matter—either through changes in biological cycling or circulation—that is not adequately captured by regressions with other properties (e.g. *S*, θ, *N*, *Si*) in Equation (5). For the 11 regressions with AOU, r_{AOU} and ΔC_{bio} are exactly 0. The remainder of the r_C signal is attributed to anthropogenic carbon uptake (ΔC_{anth}) according to equation (8):

$$\Delta C_{anth} = r_C - \Delta C_{bio} \tag{8}$$

A similar adjustment could be made using "r_A", defined analogously to ΔAOU and ΔC_T, to capture unresolved C_T changes from shifts in the calcium carbonate cycling. However, early experimentation revealed that an adjustment based on r_A had little net effect (suggesting these changes are small or well-captured by regression with *N*, AOU, or *Si*), and resulted in noisier estimates at all depths.

Sabine et al. [2008] argue the eMLR treatment is unreliable and unnecessary in the mixed layer where strong biological cycling and gas exchange decouple water mass properties and where C_{anth} increases approximately track atmospheric increases. We therefore exclude measurements in water shallower than the deepest monthly mixed layer in the mixed layer climatology of *Holte*

Deleted: Δ

Deleted: C_T

Field Code Changed

Deleted: This

Field Code Changed

Deleted: ΔC_T

Field Code Changed

Deleted: This adjustment is 0 for the 11 regressions that include AOU as a regression parameter because all AOU changes are exactly resolved when AOU is included, and ΔAOU is therefore 0. A similar adjustment could be made using "ΔA_T", defined analogously to ΔAOU and ΔC_T, to capture unresolved C_T changes from shifts in the calcium carbonate cycling. However, early experimentation revealed that an adjustment based on ΔA_T had little net effect (suggesting these changes are small or well-captured by regression with *N*, AOU, or *Si*), and resulted in noisier estimates at all depths. After removing ΔC_{bio} , the

Field Code Changed

Field Code Changed

Deleted: ΔC_T

Field Code Changed

Field Code Changed

Deleted: s

et al. (accessed Nov. 2014) from eMLR. For the mixed layer, which is better equilibrated with the atmosphere than deeper layers, anthropogenic storage is estimated in several steps. We:

1. estimate pCO_2 for the later occupation from A_T, C_T, and carbonate constants [*Dickson and Millero*, 1987];
2. subtract the increase in annual mean atmospheric pCO_2 between the earlier and later occupations according to the Mauna Loa observatory record [*Keeling*, 1986];
3. estimate C_T using the A_T measured during the later occupation and the diminished pCO_2;
4. and assume the anthropogenic storage equals the difference between the measured C_T and this lower C_T estimate.

These steps produce a ΔC_{anth} estimate at each grid location for both decades considered for each of the 16 regressions. These 16 estimates are then averaged for the final ΔC_{anth} distribution estimates. We forgo performing a weighted average because there is no solid *a priori* basis from which to determine weights for the regressions.

2.3 Column inventory change, basin storage, and overall C_{anth} estimates

C_{anth} column inventory changes are estimated in mol C m^{-2} a^{-1} by summing ΔC_{anth} over depth and dividing by the years between reoccupations. We sum from the surface to depth at which the mean ΔC_{anth} across latitude or longitude is 0.5 µmol kg^{-1}. This threshold is smaller than typical uncertainties for individual estimates (3-5 µmol kg^{-1}, see Appendix A) because we are averaging across the large number of estimates obtained at each station along a line, each of which has partially independent uncertainties. Thresholds between 0 and 1 µmol kg^{-1} return similar average results. Higher thresholds yield consistently smaller column inventory estimates, and lower thresholds return greater variability among estimates from different regressions.

Basin scale storage is estimated using the gridded World Ocean Atlas annual mean temperature and salinity data product [*Locarnini et al.*, 2013; *Zweng et al.*, 2013]. First, potential density σ_θ is calculated for each of the gridded data product locations (difficulties were encountered calculating γ^N in some nearshore environments). Next, C_{anth} changes at each location are estimated as the ΔC_{anth} on the same σ_θ surface at the same latitude along P16, normalized to a 10 year time change. The overall change is estimated as the grid cell volume-weighted sum of the ΔC_{anth}. This estimate uses only P16 because the asymmetry of the gyres in the Northern and Southern Hemispheres suggests the meridional P16 section might be better able to capture the density structure of the Pacific than the zonal P02 section. Extrapolation errors are estimated by comparing our estimates along P02 to our extrapolated estimates along P02 from P16 (Appendix A).

Overall C_{anth} is estimated for both sections in the CLIVAR and GO-SHIP decades by adding the eMLR ΔC_{anth} estimates to the WOCE-era ΔC^*-based C_{anth} estimates by *Sabine et al.*, [2002] in the GLODAPv1.1 bottle data product [*Key et al.*, 2004]. These WOCE-era ΔC^* estimates are first interpolated in the γ^N space observed during the CLIVAR and GOSHIP occupations. One or both ΔC_{anth} estimates are then added to update the overall C_{anth} estimates. Aragonite saturation state (Ω_A) and pH are calculated from the measured C_T and A_T, and the preindustrial Ω_A and pH (calculated from measured A_T and the difference between the measured C_T and estimated C_{anth}) are subtracted from them. These calculations provide an estimate of the overall impact of C_{anth} on Ω_A ($\Delta\Omega_A$) and pH (ΔpH). We linearly interpolate (and extrapolate where necessary) these estimates in time from 1991 to 2015. The overall C_{anth} estimates and a simple animation showing C_{anth} and $\Delta\Omega_A$ over time are provided as Supplementary Materials.

Errors are assessed in Appendix A. Uncertainty estimates should be considered to be ±1σ, though 95% confidence intervals are used for determining statistical significance. The error analysis reveals eMLR C_{anth} estimates vary by ±3.3 μmol kg^{-1} C_{anth} between regression coefficient sets. This uncertainty would apply in full to non-ensemble eMLR estimates that rely on a single property combination, and would be the largest single component of estimate uncertainty for such estimates. However, we argue (and show in Appendix B) this error is reduced for our 16-member ensemble eMLR. The largest remaining source of uncertainty for this analysis is then potential errors in C_T measurements or the adjustments applied to them.

Deleted: by a factor of 4 for

3. Results and Discussion

Results are presented from the surface to 1500 m depth. We do not find any statistically significant changes below this depth in the Pacific. This is expected because of the great age of most deep Pacific waters [*Matsumoto*, 2007; *Gebbie and Huybers*, 2012]. While changes in Antarctic Bottom Water C_{anth} are possible, we do not expect these changes to be detectable on decadal timescales using our methods.

3.1 r_{AOU}

We briefly examine r_{AOU} averaged for the 5 regressions (see Table 2) that did not use AOU as a regression parameter (Fig. 4). These r_{AOU} estimates are not comprehensive estimates of ΔAOU in

Deleted: *ΔAOU*

Field Code Changed

Field Code Changed

Deleted: ΔAOU

Field Code Changed

Deleted: ΔAOU

Deleted: change

a water mass because the eMLR regressions with N and Si remove the portions of ΔAOU that correlate with these nutrients, as recently pointed out by *Chu et al.* [2016]. It is therefore likely that most AOU changes from shifts in net organic matter decomposition—resulting from rain rate changes or circulation shifts—are missing from r_{AOU} estimates. We attribute the remaining r_{AOU} signal primarily to variations in organic matter export that occur near the surface and are followed by re-equilibration of O_2 and C_T (but not nutrients) with the atmosphere. Phrased differently, we believe the r_{AOU} term primarily reflects variations in *Broecker* [1974]'s quasi-conservative tracer "NO" which is oxygen adjusted for the amount of nitrate present. Since CO_2 and O_2 can both be restored to equilibrium by gas exchange, the AOU adjustment (Equation 8) remains appropriate for eMLR analyses when AOU is not used as a regression parameter.

Along both sections, our r_{AOU} estimates for the first decade (Fig. 4a and c) have a similar pattern, though of generally smaller magnitude, to the estimates obtained for the same decade by *Sabine et al.* [2008]. An exception is found for waters shallower than 400 m depth along P02, where *Sabine et al.* [2008] find consistently positive r_{AOU} and we do not. In this region their results appear dissimilar from our mean estimates, but still fall within the range of results from individual regression coefficient combinations. This apparent disagreement highlights how sensitive r_{AOU} patterns are to the choice of regression coefficients (Appendix A). Due in part to this sensitivity, most of the mean r_{AOU} estimates cannot be distinguished from 0 at >95% confidence. Another likely reason for the predominance of non-significant r_{AOU} estimates is that the majority of ΔAOU is correlated with nutrient changes and removed by our eMLR procedure.

Deleted: changes
Field Code Changed
Deleted: ΔAOU
Field Code Changed
Deleted: ΔAOU
Field Code Changed
Deleted: ΔAOU
Deleted: .
Deleted: O_2
Deleted: .
Field Code Changed
Deleted: ΔAOU
Field Code Changed
Deleted: ΔAOU
Deleted: ΔAOU
Field Code Changed
Deleted: most
Field Code Changed
Deleted: ΔAOU
Deleted: in
Field Code Changed
Deleted: value

and therefore the mean r_{AOU} estimates are small. While mostly small, significant positive r_{AOU} estimates are found near the northern and eastern edges of the P16 and P02 sections respectively in water between 26 and 27 kg m^{-3} γ^N extending between the base of the mixed layer and ~500 m. Another exception is a broadly distributed, but rarely statistically significant, positive r_{AOU} between 27 and 27.25 kg m^{-3} across P02 during the earlier decade. *Emerson et al.* [2004], *Deutsch et al.* [2006], and *Mecking et al.* [2008] attributed similar but significantly more intense changes in modeled and observed AOU along density surfaces to a decrease in ventilation of the deepest and densest (26.6 kg m^{-3} σ_θ or about 26.7 kg m^{-3} γ^N) portions of the North Pacific Subtropical Gyre. A more-direct comparison to their ΔAOU estimates can be made with 'r_{AOU}' estimates obtained using only θ and S (not shown), which were broadly 10 to 20 µmol kg^{-1} higher than our mean ensemble eMLR r_{AOU} estimates between the 26 and 27 kg m^{-3} γ^N surfaces along P02 and the northernmost portions of P16. These estimates from only θ and S, which we contend only have ΔAOU from shifts in the distributions of water masses removed, more closely match *Mecking et al.* [2008]'s findings.

Our r_{AOU} estimates are of smaller magnitude along both sections for the recent decade (Fig. 4b and d) than for the earlier decade. However, in the recent decade, r_{AOU} estimates obtained using only θ and S (not shown) were again large and positive between 25.5 and 26.7 kg m^{-3} γ^N between ~160°E and 160°W along P02, but negative east of ~140°W at densities lighter than 26 kg m^{-3} γ^N. This observation suggests waters perhaps continued to age between ~160°E and 160°W, while being partially ventilated in the shallowest and easternmost portions of the gyre (c.f. Fig. 5a and b).

Deleted: One exception

Field Code Changed

Field Code Changed

Deleted: is

Deleted: , where significant positive near-surface ΔAOU values are found

Deleted: The

Field Code Changed

Deleted: ΔAOU

Deleted: change

Field Code Changed

Deleted: ΔAOU'

Field Code Changed

Deleted: ΔAOU

Deleted: changes

Deleted: ΔAOU

Field Code Changed

Field Code Changed

Deleted: ΔAOU

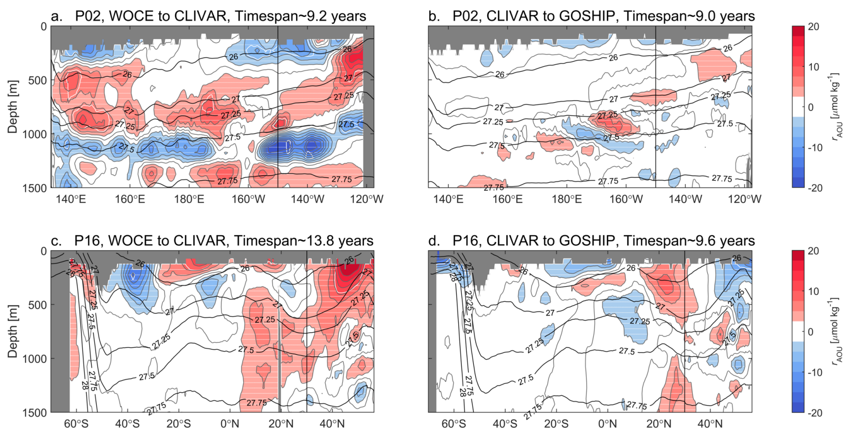

Figure 4. Sections of r_{AOU} (Equation 6), or the portions of r_{AOU} that are not removed by our eMLR method. Sections are **a.** P02 (east-west at ~30°N) in the earlier decade, **b.** P02 in the recent decade, **c.** P16 (north-south at ~150°W) in the earlier decade, and **d.** P16 in the recent decade. Thin white line hashing of changes indicates the change is not statistically significant. Vertical black lines indicate crossovers between the two sections and curved black lines indicate surfaces of constant γ^N. These estimates are only averaged for the 5 regressions that have r_{AOU} and do not include AOU as a predictor.

3.2 ΔC_{anth}

Estimates of ΔC_{anth} along the two sections for both decades (Fig. 5) reveal a familiar pattern of ΔC_{anth} of 8-13 µmol kg^{-1} near the surface extending to depth in the lower density thermocline waters of the subtropical gyres. The surface change is slightly larger in the subtropics where higher temperatures and alkalinities lead to greater CO_2 storage for a given pCO_2 change. In the interior, C_{anth} penetration is deeper in the Southern Pacific (>5 µmol kg^{-1} to at least 700 m depth

Deleted: ΔAOU
Deleted: AOU changes
Deleted: are
Field Code Changed
Field Code Changed
Field Code Changed

in both decades) where Subantarctic Mode Water (SAMW) and Antarctic Intermediate Water (AAIW) ventilate the deepest portions of the subtropical thermoclines. The less voluminous mode and intermediate water masses of the North Pacific Gyre thermocline create a shallower local ΔC_{anth} maximum in the Northern Hemisphere. Penetration is shallowest in the subpolar, subantarctic, equatorial, and eastern boundary current regions where older waters upwell that have not been as recently exposed to the atmosphere. Along P02, ΔC_{anth} broadly tracks isopycnal surfaces that shoal rapidly west of 140°E across the northward-flowing Kuroshio and gradually east of there across the generally southward-flowing gyre. An exception is found east of 160°W along P02 in the recent decade where there is a local ΔC_{anth} maximum. This exception suggests there has been an increase in ventilation along the eastern portion of P02 during the recent decade, as suggested earlier in Section 3.1 and as found along the P17N section (also in the NE Pacific) by *Chu et al.* [2016]. ΔC_{anth} extends across the thermocline, and is found in North Pacific Intermediate Water (NPIW) [*Talley*, 1993; *Yasuda*, 1997] and multiple varieties of North Pacific mode water [*Hanawa and Talley*, 2001].

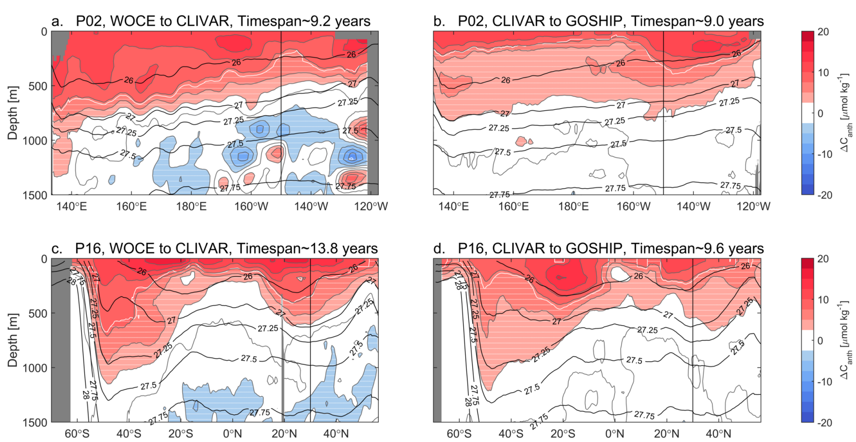

Figure 5. Sections of ΔC_{anth} (Equation 8), or estimates of the decadal increases in C_{anth} along each section. Sections are **a.** P02 (east-west at ~30°N) in the earlier decade, **b.** P02 in the recent decade, **c.** P16 (north-south at ~150°W) in the earlier decade, and **d.** P16 in the recent decade. Thin white line hashing of changes indicates the change is not statistically significant. Vertical black lines indicate crossovers between the two sections and curved black lines indicate surfaces of constant γ^N.

Deleted: our

Formatted: Font: Not Italic

Deleted: .

The ΔC_{anth} distributions agree with those found by *Sabine et al.* [2008] for the earlier decade within expected uncertainties. We find smaller C_{anth} increases in the triangle bound by [0°S at 200 m; 25°S at 200 m; and 25°S at 800 m] depth, though *Sabine et al.* [2008] also find a minimum at 20°S at ~200 m depth. Along P02, we both find local maxima near the California and Kuroshio Currents, though our Kuroshio ΔC_{anth} maximum is less pronounced than theirs. We also find higher ΔC_{anth} at the surface across P02 than they do. Disagreements between our estimates and theirs of this order (~3-5 µmol kg^{-1}, 1σ) are expected because, as *Plancherel et al.* [2013] showed and we show in Appendix A, the non-ensemble eMLR estimate distributions provided by other eMLR studies are highly sensitive to the choice of regression parameters.

Deleted: our a

Comparing ΔC_{anth} estimates for the earlier and recent decades reveals several changes in ΔC_{anth} estimate patterns. To quantify these shifts, we normalize the ΔC_{anth} distributions to a 10-year timespan and then directly difference them ($\Delta\Delta C_{anth}$, for a change in the change, in Fig. 6). The largest statistically significant feature is a large increase in ΔC_{anth} in densities between the 26 kg m^{-3} iso-neutral surface and the base of the mixed layers between 30°S and 10°S along P16. A second broad ΔC_{anth} decrease can be seen along P02 in densities lighter than 26 kg m^{-3} γ^N west of

160°W (and somewhat deeper further west). While these ΔC_{anth} changes along P02 are rarely statistically significant individually, they are collectively a distinguishable feature. In Sections 3.3 and 3.5, we rule out the possibility that either of these changes result from shifts in the locations of water masses, so we attribute them instead to changes in the degree of ventilation of water masses at these locations. A likely explanation for the South Pacific storage change increase is variability in the overturning of the Southern Pacific Subtropical Cell (STC), which transports water equatorward along the ~25 kg m^{-3} γ^N isoneutral surface, where this feature is at a maximum. The STC exhibits substantial decadal variability, and was declining prior to 1998 [*McPhaden and Zhang*, 2002] before rebounding [*McPhaden and Zhang*, 2004] and intensifying through the recent decade [*England et al.*, 2014]. The (barely statistically significant) portions of this signal in waters denser than 26 kg m^{-3} γ^N may be due to an intensification of SAMW formation in the earlier decade [*Waugh et al.*, 2013], that, sustained in the recent decade, is now propagating further North.

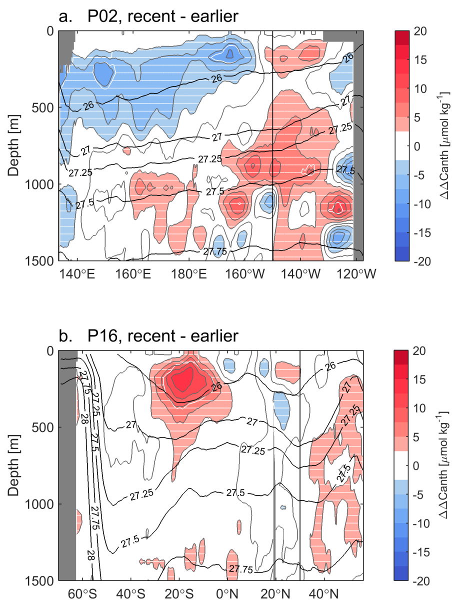

Figure 6. Differences between decadal uptake of C_{anth} in the recent and earlier decades considered ($\Delta\Delta C_{anth}$). These estimates are calculated directly along **a.** P02 (east-west at ~30°N) and **b.** P16 (north-south at ~150°W). Thin white hashing of changes indicates the change is not statistically significant. Vertical black lines indicate crossovers between the two sections and curved black lines indicate surfaces of constant γ^N.

3.3 ΔC_{anth} variability

While eMLR removes the effects of many forms of sub-decadal variability on C_T, the method does not also remove all sub-decadal variability in C_{anth}. For example, *Woosley et al.*, [2016] used eMLR to show mesoscale eddies redistribute C_{anth} along sections. Water mass redistributions such as eddies and frontal shifts can appear in ΔC_{anth} estimates when the eMLR regressions are applied to property distributions that were measured in shifting water masses (i.e.

P in Equation 2). For example, a passing eddy during a hydrographic occupation would rearrange the density structure of the water being measured and result in a redistribution of the physical and biogeochemical measurements used in equations (5 and 6). We estimate the impact of this variability on ΔC_{anth} estimates as the differences between estimates obtained from different property distributions (i.e. using *P* from a different decade). Expressed in the notation of Equation (2), we estimate this term as:

$$\text{"Variability"}\ \Delta \mathrm{C}_{\mathrm{anth}} = f_2(P_2) - f_1(P_2) - (f_2(P_1) - f_1(P_1)) \qquad (9)$$

for a WOCE to CLIVAR comparison. This "Variability" ΔC_{anth} estimate averages (mean±r.m.s.) 0.1±0.9 µmol kg^{-1} between the base of the mixed layer and 1500 m depth in our four sets of estimates, suggesting it is a small contribution to overall ΔC_{anth} estimate variability. However, eMLR can fail to identify local ΔC_{anth} variability when determining regression coefficients with measurements made over broad areas. Therefore this analysis does not rule out such variability meaningfully redistributing C_{anth}, it merely suggests a small role for such variability in governing eMLR ΔC_{anth} estimates.

3.4 Column inventory change rates

As shown in Section 3.2, ΔC_{anth} is greatest in low-density recently ventilated thermocline waters. C_{anth} column inventory increases (Fig. 7) are therefore greatest along P02 in the earlier decade in the Eastern Pacific where isopycnal surfaces are deepest. A similar pattern is seen along P02 in the recent decade though the region of elevated increases east of 160°W noted in section 3.2 is also apparent. Mean column inventory stayed approximately constant at 0.53±0.11 and 0.46±0.11 mol C m^{-2} a^{-1} along P02 in the earlier and recent decades, respectively. Along P16 there is a double hump characteristic of the deeper penetration of low density mode and

Deleted: from

Formatted: Font: Italic

Formatted: Font color: Auto

Deleted: ¶

Deleted: 12

Deleted: 12

intermediate water types in the North and South Pacific Gyres than in the surrounding Antarctic, Subpolar, and Equatorial Pacific. A similar pattern is seen in the recent decade along P16, though a new local column storage maximum at ~20°S is also visible. Mean C_{anth} storage along P16 increased slightly from 0.29±0.10 to 0.45±0.11 mol C m^{-2} a^{-1} in the earlier and recent decades, respectively. This change was driven by a statistically significant C_{anth} storage acceleration from 0.36±0.10 to 0.58±0.10 mol C m^{-2} a^{-1} in the South Pacific, and a comparable or increasing North Pacific storage of 0.23±0.1 and 0.31±0.1 mol C m^{-2} a^{-1} in the earlier and recent decades, respectively.

The lighter blue bands in Fig. 7 indicate the overall uncertainty estimates (1σ) for our eMLR method (see Appendix A). A major source of the overall uncertainty for traditional eMLR and ensemble eMLR is uncertainty in the C_T measurements or measurement adjustments (Section 2.1), where a 1 μmol kg^{-1} error over 10 years—integrated over 1000 m of seawater—creates a ~0.1 mol m^{-2} a^{-1} storage change error. With these large uncertainties, it is difficult to conclude whether shifts in column storage are real, especially because errors in adjustments derived from CLIVAR era measurements could have opposing effects on the two decadal records, amplifying the apparent differences. Nevertheless, the largest apparent change is more than double the overall uncertainty; at 15.75°S, the decadal column inventory increase grew from 0.15 to 0.61 mol C m^{-2} a^{-1}. The second largest changes are the increases noted along the eastern portion of P02. As discussed throughout Section 3, we attribute these two features primarily to shifts in the degree of ventilation of these water masses.

The orange dotted lines in Fig. 7 show column inventory estimates obtained from ΔC_{anth} estimates created from the property distributions of the CLIVAR decades instead of the GO-SHIP decades (see Section 3.3). The broad similarity between the orange and black dotted lines on average reinforces the idea that shifts in the locations of water masses alone cannot account for the regional shifts in ventilation seen near 20°S along P16 or in the Eastern Pacific along P02. Shifts in the degree of ventilation of water masses are therefore a more likely explanation. The differences between the orange and black dotted lines show the effects of decadal and shorter-term variability on the C_{anth} distributions (e.g. eddies and frontal shifts).

Deleted: green

Deleted: 7b and d

Deleted: green

Deleted: and black

Deleted: green

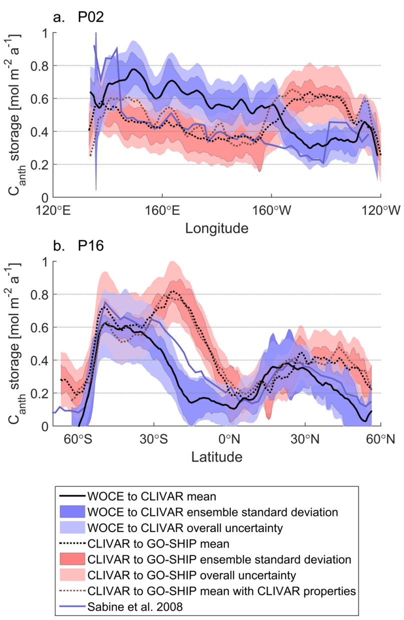

Figure 7. Column C_{anth} inventory changes. Panels are for **a.** P02 (east-west at ~30°N) and **b.** P16 (north-south at ~150°W). Light blue and red shading around black lines (ensemble

Deleted: in the earlier decade

Deleted: ,

Deleted: P02

Deleted: in the recent decade, **c.** P16

Deleted:) in the earlier decade, and **d.** P16 in the recent decade means) indicate the overall uncertainties on our estimates. Dark blue and red shading indicates the standard deviation between ensemble members. Solid blue lines are estimates from *Sabine et al.* [2008] for the same sections and earlier WOCE to CLIVAR decades. Orange dotted lines provided for comparison with the black lines, are estimates of the column inventory change rates calculated using the CLIVAR era property distributions instead of the GO-SHIP era distributions. We argue the differences between the orange and black dotted lines represent the effects of sub-decadal redistribution of C_{anth} (Section 3.3).

Our estimates from the earlier decade generally match estimates in the literature to within uncertainties. *Sabine et al.* [2008] estimated column inventories with eMLR along both of these sections, so we plot their results directly with ours (solid blue lines in Fig. 7). Considering P02 and P16 results collectively, their results and ours agree to within uncertainties (i.e. the blue lines are within the light blue windows for >68% of the two panels). *Williams et al.* [2015] also used eMLR to estimate column inventories along S4P in the Pacific sector of the Southern Ocean (67°S) over the period spanning both of the decades considered, and found an average of 0.1 mol C m^{-2} a^{-1}. Our nearest estimates along P16 that span both decades (at 62.5°S) average 0.06±0.1 C m^{-2} a^{-1}. *Murata et al.* [2007] used the ΔnC_T^{CAL} method—which uses a collection of assumptions in lieu of empirical relationships to adjust for the influences of natural variability—to estimate column C_{anth} inventories along P06, which crosses P16 at 32°S and spans a similar time period to our earlier decade. They find a C_{anth} storage of 0.64±~0.4 mol C m^{-2} a^{-1} west of P16 and 1.25±~0.4 C mol m^{-2} a^{-1} east of P16. Our estimate of 0.53±0.11 mol C m^{-2} a^{-1} is within uncertainties of one of these estimates and is lower than the other. *Chu et al.* [2016] estimate C_{anth} changes along P17N between 2001 and 2012. The P17N section angles from near P16 at

Deleted: Orange

Deleted: lines in **a.** and **b.**

Deleted: time

Deleted: period

Deleted: Green

Deleted: in panels **b**. and **d.**,

Deleted: green

Deleted: a and c

Deleted: in orange

Deleted: The *Sabine et al.* [2008] estimates are generally within 1 ensemble standard deviation of ours, suggesting their results can be thought of as another member of our ensemble

~50°N to near P02 at 135°W. *Chu et al.* [2016]'s estimates decrease from 0.55±0.12 mol m^{-2} a^{-1} at 34°N to ~0.2±0.12 m^{-2} a^{-1} at 50°N, while the nearest estimates on our sections in the recent decades are 0.50±0.11 mol m^{-2} yr^{-1} and 0.35±0.11 mol m^{-2} yr^{-1}, respectively. They attribute differences between their estimates and the estimates of *Sabine et al.* [2008] along P16 and P02 to differences in methods used and regions considered. Our results confirm the importance of such methodological differences, and also suggest that differences in the timeframes considered are also likely important.

3.5 Basin inventory changes

Basin inventory change estimates are averaged by 10° latitude bands and by hemispheres in Table 3. Pacific C_{anth} storage increased on average from 6.1±1.6 to 8.9±2.2 PgC $decade^{-1}$. By comparison, *Woosley et al.* [2016] found anthropogenic carbon storage also increased in the recent decade in the North Atlantic, leading to an overall Atlantic storage increase from 5.1 to 8.1 PgC $decade^{-1}$. Pacific storage is comparable to Atlantic storage—despite the formation of North Atlantic Deep Water in the Atlantic—because of the larger volume of the Pacific Ocean. The Pacific storage increase between the earlier and the later decades was primarily driven by a large increase in Southern Pacific storage from 3.8±1.0 to 6.8±1.7 PgC $decade^{-1}$. The North Pacific inventory increase remained constant to within uncertainties at 2.4±0.6 PgC $decade^{-1}$ in the earlier and 2.8±0.6 PgC $decade^{-1}$ in the later decade. Pacific decadal storage increases outpaced the slightly increased rate of atmospheric CO_2 accumulation. The increases in Southern Pacific storage estimates cannot be explained by variability in the depths of isopycnal surfaces because both of these estimates were extrapolated onto the same World Ocean Atlas climatological density field. This suggests changes in ventilation, or displacement of water masses with differing degrees of ventilation, also occurred. We note that our decadal basin and latitude band inventory estimates might be overestimates if any shifts were unique to the time or longitude windows around the GO-SHIP P16 occupation (e.g. related to El Niño or the Blob [*Amaya et al.*, 2016]). Upcoming reoccupations of the P15 (170°W), P06 (~30°S), and P18 (103°W) lines will afford the opportunity to test temporal and regional extent of these changes, and will provide means to reduce the uncertainties associated with these extrapolations from only a single section. There are re-occupied sections that could be analyzed in the Northern Pacific as well, including P14 (180°E).

Table 3. Pacific decadal C_{anth} storage for the latitude bands spanned by P16 in Pg C decade^{-1}. The "total" values include estimates for (not shown) data-poor latitude bands from 60°N to 67°N and 70°S to 80°S, and therefore do not exactly equal the sum of all rows.

Latitude Band	WOCE to CLIVAR	CLIVAR to GOSHIP
70 to 60°S	†	0.65
60 to 50°S	0.56	0.84
50 to 40°S	0.90	0.97
40 to 30°S	0.96	1.07
30 to 20°S	0.65	1.31
20 to 10°S	0.35	1.20
10 to 0°S	0.29	0.72
0 to 10°N	0.46	0.56
10 to 20°N	0.79	0.52
20 to 30°N	0.60	0.64
30 to 40°N	0.35	0.53
40 to 50°N	0.13	0.35
50 to 60°N	0.07	0.21
S. Hemisphere	3.8±1.0	6.8±1.7
N. Hemisphere	2.4±0.6	2.8±0.7
Total (60°S to 60°N)	6.1±1.6	8.9±2.2

† insufficient data

3.6 Overall C_{anth} and impacts on pH and aragonite saturation

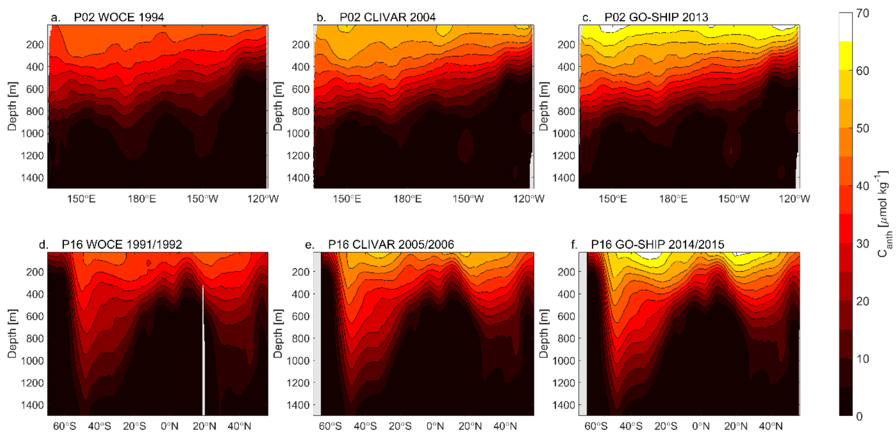

Figure 8. Estimates of total C_{anth} accumulation since the preindustrial era. Sections are **a.** P02 (east-west at ~30°N) in the WOCE occupation, **b.** P02 in the CLIVAR occupation, **c.** P02 in the GOSHIP occupation, **d.** P16 (north-south at ~150°W) in the WOCE occupation, **e.** P16 in the CLIVAR occupation, and **f.** P16 in the GOSHIP occupation.

C_{anth} distributions have been steadily increasing throughout the gyre thermoclines of the Pacific (Fig. 8). The highest concentrations of 65 to 70 μmol kg^{-1} C_{anth} are found in the surface ocean in the GO-SHIP occupations, corresponding the approximate expected increase from equilibration with a changing atmosphere (assuming seawater at ~20 °C with a salinity of 33, an A_T 2200, and a pCO_2 increase from 280 to 400 ppm). Surface concentrations fall at higher latitudes where colder seawater temperatures correspond to less C_{anth} gain for a given atmospheric change. C_{anth} concentrations fall also with depth. In the interior, C_{anth} becomes a passive tracer, and distributions broadly track the isopycnal surfaces along which advection and diffusion are strongest. Upwelling lifts isopycnal surfaces, decreasing C_{anth} along, for example, equatorial latitudes and the U.S. West Coast.

Table 4. Net impacts of ocean acidification since the preindustrial era on surface aragonite mineral saturation ($\Delta\Omega_A$) and pH (ΔpH) estimated for latitude bands along P16 (running north-south at ~150°W) in 1994, 2004, and 2014. Uncertainties on these estimates are small (5-10%), but we do not account for unknown potential errors in our presumption of fixed average surface atmospheric disequilibrium since the WOCE occupation.

Latitude Band	$\Delta\Omega_A$ 1994	$\Delta\Omega_A$ 2004	$\Delta\Omega_A$ 2014	ΔpH 1994	ΔpH 2004	ΔpH 2014
60 to 50°S	-0.29	-0.32	-0.39	-0.09	-0.10	-0.13
50 to 40°S	-0.56	-0.67	-0.78	-0.10	-0.12	-0.14
40 to 30°S	-0.57	-0.69	-0.82	-0.08	-0.10	-0.12
30 to 20°S	-0.52	-0.65	-0.79	-0.07	-0.09	-0.11
20 to 10°S	-0.44	-0.54	-0.70	-0.06	-0.07	-0.09
10 to 0°S	-0.44	-0.51	-0.60	-0.06	-0.07	-0.08
0 to 10°N	-0.47	-0.54	-0.63	-0.07	-0.08	-0.09
10 to 20°N	-0.52	-0.63	-0.74	-0.07	-0.09	-0.10
20 to 30°N	-0.54	-0.67	-0.80	-0.07	-0.09	-0.11
30 to 40°N	-0.55	-0.65	-0.77	-0.08	-0.10	-0.12
40 to 50°N	-0.49	-0.59	-0.69	-0.09	-0.11	-0.13
50 to 60°N	-0.41	-0.50	-0.57	-0.09	-0.12	-0.14
Average all lats.	-0.48	-0.58	-0.69	-0.08	-0.09	-0.11

As expected [*Doney et al.*, 2009; *Feely et al.*, 2009, 2012], C_{anth} storage has continued to acidify the ocean and decrease carbonate mineral saturations. Aragonite saturation decreases from C_{anth} storage increased in approximate proportion to the C_{anth} concentrations stored since the preindustrial era ($\Delta\Omega_A$ in Fig. 9**d**, **e**, and **f**), while changes in pH were more complex (ΔpH in Fig. 9**a**, **b**, and **c**). Net surface $\Delta\Omega_A$ ranged between -0.41 and -0.57 in 1994 and between -0.57 and -0.82 in 2014 (Table 4), while surface ΔpH ranged from -0.06 to -0.10 in 1994 and from -0.08 to -0.14 in 2014. Surface aragonite saturation (and pH) fell at an average rate of 0.29% (0.020%) per year and 0.34% (0.023%) per year in the earlier and recent decades, respectively.

The acceleration of these surface acidification signals is due to accelerating atmospheric CO_2 concentration increases.

Understanding pH and Ω_A change variability with latitude (along P16 in Table 4) and with depth (Fig. 9) requires understanding two properties of the carbonate system in seawater: First, colder seawater holds more C_T at a given pCO_2 or pH, and has lower Ω_A. Second, the higher the C_T of seawater, the less a given change in pCO_2 will change C_T and Ω_A. High-latitude surface waters that are naturally rich in C_T due to cold temperatures (e.g. polar surface seawater) exhibit smaller changes in Ω_A. Similarly, upwelling regions (e.g. equatorial surface seawater) also exhibit a smaller Ω_A decreases for a fixed pCO_2 changes than warm low-C_T surface waters (e.g. subtropical surface waters). This accounts for the two Ω_A change maxima at mid-latitudes in Table 4. The sensitivity of pH to a changing atmospheric pCO_2 increases as temperature decreases whereas the opposite is true for Ω_A. For this reason, the magnitude of ΔpH reaches local maxima rather than local minima in cold high-latitude waters. Anthropogenic changes in pH are amplified at depth where pH is naturally lower—implying a larger change in pCO_2 and pH for a given change in C_T—and where there is no contact with the atmosphere to hold pCO_2 near the atmospheric value. For this reason, the largest pH decreases are at ~500 m depth (Fig. 9) where high near-surface C_{anth} storages combine with elevated subsurface C_T from biological remineralization. The large variability of the ΔpH signal can be attributed to the strong sensitivity of ΔpH to the naturally variable C_T distribution (c.f. Fig. 2). There is no comparable amplification for $\Delta\Omega_A$, which exhibits more laterally homogenous distributions (Fig. 9).

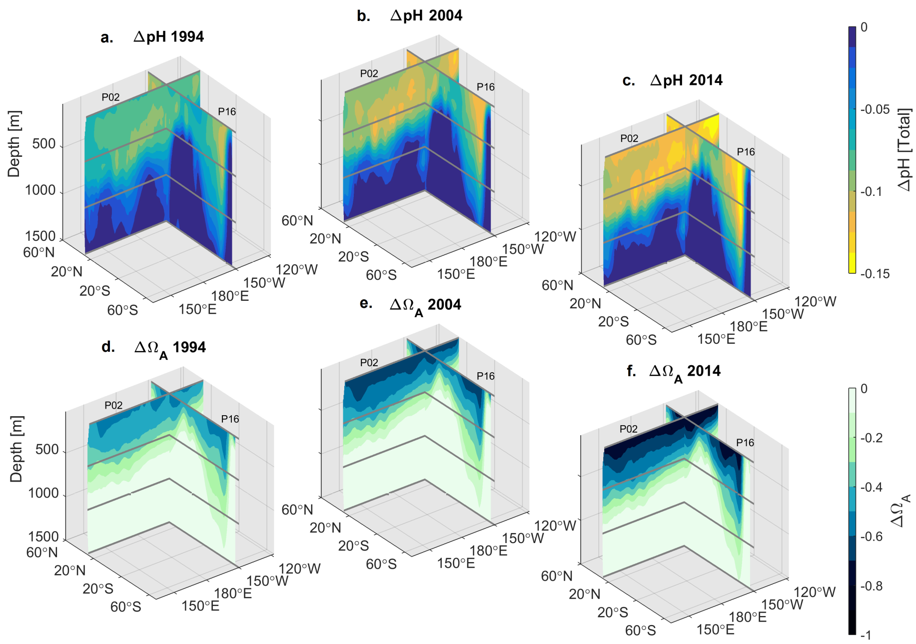

Figure 9. 3D sections of the net impact of ocean acidification on pH (total scale, panels **a** through **c**) and aragonite saturation ($\Delta\Omega_A$, panels **d** through **f**) along P02 (sections from lower left to upper right) and P16 (sections from upper left to lower right) from the preindustrial era to (**a.** and **e.**) 1994, (**b.** and **d.**) 2004 and (**c.** and **f.**) 2014.

Conclusions

We have used a modified eMLR method to estimate two decades of anthropogenic carbon storage along the P02 (east-west at ~30°N) and P16 (north-south at ~150°W) sections. C_{anth} storage increased in the Pacific Ocean from 6.1±1.5 to 8.9±2.2 PgC decade^{-1} between 60°N and 60°S, due largely to storage increases in the Southern Pacific. The increase in the rate of storage in the South Pacific is attributed to increased ventilation of the Pacific Subtropical Cell. Decadal storage was smaller west of 160°W along P02 in the recent decade, and slightly higher east of there. This may be due to continued changes in the ventilation of the North Pacific Gyre thermocline. This hypothesis could be tested by examining changes in chlorofluorocarbon distributions and AOU. By 2014, C_{anth} storage had changed Pacific surface Ω_A and pH by an average of -0.69 and -0.11, respectively.

We adapted the eMLR method to quantify and reduce the impact on our estimates of several semi-arbitrary methodological choices. The primary modification is to use an ensemble of regression coefficients instead of a single set. We have tested our modified methods using model outputs with known values and found each modification yields improved estimates. We also demonstrate the value of our ensemble approach for estimating a subset of uncertainties inherent to the eMLR method. Finally, we have demonstrated that our methods return similar estimates to within expected uncertainties to estimates from eMLR given in literature.

One weakness of our study is the need to extrapolate across the Pacific Ocean from just two sections in order to infer basin inventory changes. A greatly improved estimate of Pacific basin inventories will be possible following the completion of, for example, the P18, P15, and P06 lines planned for 2016 and 2017. Estimates of C_{anth} changes along these lines would also provide means to assess the spatial and temporal extent of the C_{anth} storage patterns observed.

Acknowledgements

Deleted: hile w

Deleted: not yet

Deleted: , we have demonstrated that our methods return similar estimates to within expected uncertainties to estimates from eMLR given in literature.

All data used can be accessed at http://cchdo.ucsd.edu/. Anthropogenic carbon estimates generated in this research are available as a supplement. This research would not be possible without the hard work of the scientists and crew aboard the RVs Revelle, Palmer, Brown, Discoverer, Washington, Thompson, Knorr, and Kaiyo-Maru. We thank funding agencies and program managers: BRC was supported by the Carbon Data Management and Synthesis NOAA grant (N8R1SE3-PGC) managed by Kathy Tedesco. AMM was supported by NOAA grant NA11OAR4310063. The support of KBR comes through awards NA17RJ2612 and A08OAR4320752, including support through the NOAA Office of Climate Observations, NOAA award NA11OAR4310066. This is PMEL contribution number 4519 and JISAO contribution number 2016-01-22.

Formatted: Space After: 8 pt

Formatted: Font: 12 pt

Formatted: Font: 12 pt

Formatted: Font: 12 pt

Formatted: Font:

References

Amaya, D. ., N. E. Bond, J. A. Miller, and M. J. DeFlorio (2016), The evolution and known atmospheric forcing mechanisms behind the 2013-2015 North Pacific warm anomalies, *US CLIVAR Var. Newsl.*, *14*(2), 1–6.

Anderson, J. L. et al. (2004), The new GFDL global atmosphere and land model AM2-LM2: Evaluation with prescribed SST simulations, *J. Clim.*, *17*(24), 4641–4673.

Anderson, L. A., and J. L. Sarmiento (1994), Redfield ratios of remineralization determined by nutrient data analysis, *Global Biogeochem. Cycles*, *8*(1), 65–80, doi:10.1029/93GB03318.

Böning, C. W., A. Dispert, M. Visbeck, S. R. Rintoul, and F. U. Schwarzkopf (2008), The response of the Antarctic Circumpolar Current to recent climate change, *Nat. Geosci.*, *1*(12), 864–869, doi:10.1038/ngeo362.

Broecker, W. S. (1974), "NO", a conservative water-mass tracer, *Earth Planet. Sci. Lett.*, *23*(1),

100–107, doi:10.1016/0012-821X(74)90036-3.
Canadell, J. G., C. Le Quéré, M. R. Raupach, C. B. Field, E. T. Buitenhuis, P. Ciais, T. J. Conway, N. P. Gillett, R. A. Houghton, and G. Marland (2007), Contributions to accelerating atmospheric CO_2 growth from economic activity, carbon intensity, and efficiency of natural sinks., *Proc. Natl. Acad. Sci. U. S. A.*, *104*(47), 18866–70, doi:10.1073/pnas.0702737104.
Carter, B. R., J. R. Toggweiler, R. M. Key, and J. L. Sarmiento (2014), Processes determining the marine alkalinity and calcium carbonate saturation state distributions, *Biogeosciences*, *11*(24), 7349–7362, doi:10.5194/bg-11-7349-2014.
Carter, B. R., N. L. Williams, A. R. Gray, and R. A. Feely (2016a), Locally interpolated alkalinity regression for global alkalinity estimation, *Limnol. Oceanogr. Methods*, *14*(4), 268–277, doi:10.1002/lom3.10087.
Carter, B. R., T. L. Frölicher, J. P. Dunne, K. B. Rodgers, R. D. Slater, and J. L. Sarmiento (2016b), When can ocean acidification impacts be detected from decadal alkalinity measurements?, *Global Biogeochem. Cycles*, *30*(4), 595–612, doi:10.1002/2015GB005308.
Chu, S. N., Z. A. Wang, S. C. Doney, G. L. Lawson, and K. A. Hoering (2016), Changes in anthropogenic carbon storage in the Northeast Pacific in the last decade, *J. Geophys. Res. Ocean.*, doi:10.1002/2016JC011775.
Deutsch, C., S. Emerson, and L. Thompson (2006), Physical-biological interactions in North Pacific oxygen variability, *J. Geophys. Res.*, *111*(C9), C09S90, doi:10.1029/2005JC003179.
Dickson, A. G., and F. J. Millero (1987), A comparison of the equilibrium constants for the dissociation of carbonic acid in seawater media, *Deep Sea Res. Part A. Oceanogr. Res. Pap.*, *34*(10), 1733–1743, doi:10.1016/0198-0149(87)90021-5.

Doney, S. C., V. J. Fabry, R. A. Feely, and J. A. Kleypas (2009), Ocean acidification: the other CO2 problem., *Ann. Rev. Mar. Sci.*, *1*, 169–92, doi:10.1146/annurev.marine.010908.163834.

Dunne, J. P. et al. (2013), GFDL's ESM2 Global Coupled Climate–Carbon Earth System Models. Part II: Carbon System Formulation and Baseline Simulation Characteristics, *J. Clim.*, *26*(7), 2247–2267, doi:10.1175/JCLI-D-12-00150.1.

Durack, P. J., S. E. Wijffels, and R. J. Matear (2012), Ocean salinities reveal strong global water cycle intensification during 1950 to 2000., *Science*, *336*(6080), 455–8, doi:10.1126/science.1212222.

Emerson, S., Y. W. Watanabe, T. Ono, and S. Mecking (2004), Temporal Trends in Apparent Oxygen Utilization in the Upper Pycnocline of the North Pacific: 1980–2000, *J. Oceanogr.*, *60*(1), 139–147, doi:10.1023/B:JOCE.0000038323.62130.a0.

England, M. H., S. McGregor, P. Spence, G. A. Meehl, A. Timmermann, W. Cai, A. Sen Gupta, M. J. McPhaden, A. Purich, and A. Santoso (2014), Recent intensification of wind-driven circulation in the Pacific and the ongoing warming hiatus, *Nat. Clim. Chang.*, *4*(3), 222–227, doi:10.1038/nclimate2106.

Feely, R., S. Doney, and S. Cooley (2009), Ocean Acidification: Present Conditions and Future Changes in a High-CO2 World, *Oceanography*, *22*(4), 36–47, doi:10.5670/oceanog.2009.95.

Feely, R. A., C. L. Sabine, R. H. Byrne, F. J. Millero, A. G. Dickson, R. Wanninkhof, A. Murata, L. A. Miller, and D. Greeley (2012), Decadal changes in the aragonite and calcite saturation state of the Pacific Ocean, *Global Biogeochem. Cycles*, *26*(3), doi:10.1029/2011GB004157.

Friis, K., A. Körtzinger, J. Pätsch, and D. W. R. Wallace (2005), On the temporal increase of anthropogenic CO_2 in the subpolar North Atlantic, *Deep Sea Res. Part I Oceanogr. Res. Pap.*, *52*(5), 681–698, doi:10.1016/j.dsr.2004.11.017.

Gattuso, J. P., and R. A. Feely (2016), *Future of the Ocean and its Seas: a non-governmental scientific perspective on seven marine research issues of G7 interest.*, Paris.

Gattuso, J.-P. et al. (2015), OCEANOGRAPHY. Contrasting futures for ocean and society from different anthropogenic CO_2 emissions scenarios., *Science*, *349*(6243), aac4722, doi:10.1126/science.aac4722.

Gebbie, G., and P. Huybers (2012), The Mean Age of Ocean Waters Inferred from Radiocarbon Observations: Sensitivity to Surface Sources and Accounting for Mixing Histories, *J. Phys. Oceanogr.*, *42*(2), 291–305, doi:10.1175/JPO-D-11-043.1.

Goodkin, N. F., N. M. Levine, S. C. Doney, and R. Wanninkhof (2011), Impacts of temporal CO_2 and climate trends on the detection of ocean anthropogenic CO_2 accumulation, *Global Biogeochem. Cycles*, *25*(3), n/a–n/a, doi:10.1029/2010GB004009.

Griffies, S., M. Schmidt, and M. Herzfeld (2009), *Elements of mom4p1*, Princeton, NJ.

Hanawa, K., and L. Talley (2001), Mode waters, *Int. Geophys. Ser.*

Jackett, D. R., and T. J. McDougall (1997), A Neutral Density Variable for the World's Oceans, *J. Phys. Oceanogr.*, *27*(2), 237–263, doi:10.1175/1520-0485(1997)027<0237:ANDVFT>2.0.CO;2.

Keeling, C. D. (1986), *Atmospheric CO2 Concentrations - Mauna Loa Observatory, Hawaii 1958-1986*, Oak Ridge National Laboratory.

Key, R. M., A. Kozyr, C. L. Sabine, K. Lee, R. Wanninkhof, J. L. Bullister, R. A. Feely, F. J. Millero, C. Mordy, and T.-H. Peng (2004), A global ocean carbon climatology: Results from Global Data Analysis Project (GLODAP), *Global Biogeochem. Cycles*, *18*(4), 1–23, doi:10.1029/2004GB002247.

Khatiwala, S., F. Primeau, and T. Hall (2009), Reconstruction of the history of anthropogenic CO_2 concentrations in the ocean., *Nature*, *462*(7271), 346–9, doi:10.1038/nature08526.

Levine, N. M., S. C. Doney, R. Wanninkhof, K. Lindsay, and I. Y. Fung (2008), Impact of ocean carbon system variability on the detection of temporal increases in anthropogenic CO_2, *J. Geophys. Res.*, *113*(C3), C03019, doi:10.1029/2007JC004153.

Locarnini, R. A. et al. (2013), World Ocean Atlas 2013. Vol. 1: Temperature., *S. Levitus, Ed.; A. Mishonov, Tech. Ed.; NOAA Atlas NESDIS*, *73*(September), 40, doi:10.1182/blood-2011-06-357442.

Matsumoto, K. (2007), Radiocarbon-based circulation age of the world oceans, *J. Geophys. Res.*, *112*(C9), C09004, doi:10.1029/2007JC004095.

McPhaden, M. J., and D. Zhang (2002), Slowdown of the meridional overturning circulation in the upper Pacific Ocean, *Nature*, *415*(6872), 603–608, doi:10.1038/415603a.

McPhaden, M. J., and D. Zhang (2004), Pacific Ocean circulation rebounds, *Geophys. Res. Lett.*, *31*(18), L18301, doi:10.1029/2004GL020727.

Mecking, S., C. Langdon, R. A. Feely, C. L. Sabine, C. A. Deutsch, and D.-H. Min (2008), Climate variability in the North Pacific thermocline diagnosed from oxygen measurements: An update based on the U.S. CLIVAR/CO 2 Repeat Hydrography cruises, *Global Biogeochem. Cycles*, *22*(3), 1–11, doi:10.1029/2007GB003101.

Morgan, P., and L. Pender (2006), CSIRO Marine Research MATLAB Seawater Software Library, Available from: http://www.marine.csiro.au/marq/edd_search.Browse_Citation?txtSession=6438&brief=Y (Accessed 12 March 2016)

Murata, A., Y. Kumamoto, S. Watanabe, and M. Fukasawa (2007), Decadal increases of anthropogenic CO_2 in the South Pacific subtropical ocean along 32°S, *J. Geophys. Res.*, *112*(C5), C05033, doi:10.1029/2005JC003405.

Pfister, C. A. et al. (2014), Detecting the unexpected: a research framework for ocean acidification., *Environ. Sci. Technol.*, *48*(17), 9982–94, doi:10.1021/es501936p.

Plancherel, Y., K. Rodgers, R. Key, A. Jacobson, and J. Sarmiento (2013), Role of regression model selection and station distribution on the estimation of oceanic anthropogenic carbon change by eMLR, *Biogeosciences*, *10*(7), 4801–4831, doi:10.5194/bg-10-4801-2013.

Purkey, S. G., and G. C. Johnson (2010), Warming of Global Abyssal and Deep Southern Ocean Waters between the 1990s and 2000s: Contributions to Global Heat and Sea Level Rise Budgets, *J. Clim.*, *23*(23), 6336–6351, doi:10.1175/2010JCLI3682.1.

Purkey, S. G., and G. C. Johnson (2013), Antarctic Bottom Water Warming and Freshening: Contributions to Sea Level Rise, Ocean Freshwater Budgets, and Global Heat Gain, *J. Clim.*, *26*(16), 6105–6122, doi:10.1175/JCLI-D-12-00834.1.

Le Quéré, C., R. Moriarty, R. M. Andrew, G. P. Peters, P. Ciais, P. Friedlingstein, and S. D. Jones (2015), Global carbon budget 2014, *Earth Syst. Sci. Data*, *7*(1), 47–85, doi:10.5194/essd-7-47-2015.

Sabine, C. L., R. A. Feely, R. M. Key, J. L. Bullister, F. J. Millero, K. Lee, T.-H. Peng, B. Tilbrook, T. Ono, and C. S. Wong (2002), Distribution of anthropogenic CO_2 in the Pacific Ocean, *Global Biogeochem. Cycles*, *16*(4), 30–1–30–17, doi:10.1029/2001GB001639.

Sabine, C. L. et al. (2004), The oceanic sink for anthropogenic CO_2., *Science*, *305*(5682), 367–71, doi:10.1126/science.1097403.

Sabine, C. L., R. A. Feely, F. J. Millero, A. G. Dickson, C. Langdon, S. Mecking, and D. Greeley

(2008), Decadal changes in Pacific carbon, *J. Geophys. Res.*, *113*(C7), C07021, doi:10.1029/2007JC004577.

Talley, L. D. (1993), Distribution and Formation of North Pacific Intermediate Water, *J. Phys. Oceanogr.*, *23*(3), 517–537, doi:10.1175/1520-0485(1993)023<0517:DAFONP>2.0.CO;2.

Velo, A., F. F. Pérez, T. Tanhua, M. Gilcoto, A. F. Ríos, and R. M. Key (2013), Total alkalinity estimation using MLR and neural network techniques, *J. Mar. Syst.*, *111-112*, 11–18, doi:10.1016/j.jmarsys.2012.09.002.

Wallace, D. (1995), *Monitoring Global Ocean Carbon Inventories*, College Station, TX.

Wanninkhof, R., S. C. Doney, J. L. Bullister, N. M. Levine, M. Warner, and N. Gruber (2010), Detecting anthropogenic CO 2 changes in the interior Atlantic Ocean between 1989 and 2005, *J. Geophys. Res.*, *115*(C11), C11028, doi:10.1029/2010JC006251.

Waugh, D. W., T. M. Hall, B. I. McNeil, R. Key, and R. J. Matear (2006), Anthropogenic CO 2 in the oceans estimated using transit time distributions, *Tellus B*, *58*(5), 376–389, doi:10.1111/j.1600-0889.2006.00222.x.

Waugh, D. W. et al. (2013), Recent changes in the ventilation of the southern oceans., *Science*, *339*(6119), 568–70, doi:10.1126/science.1225411.

Williams, N. L., R. A. Feely, C. L. Sabine, A. G. Dickson, J. H. Swift, L. D. Talley, and J. L. Russell (2015), Quantifying anthropogenic carbon inventory changes in the Pacific sector of the Southern Ocean, *Mar. Chem.*, *174*, 147–160, doi:10.1016/j.marchem.2015.06.015.

Woosley, R. J., F. J. Millero, and R. Wanninkhof (2016), Rapid Anthropogenic Changes in CO 2 and pH in the Atlantic Ocean: 2003-2014, *Global Biogeochem. Cycles*, *30*, 1–21, doi:10.1002/2015GB005248.

Yasuda, I. (1997), The origin of the North Pacific Intermediate Water, *J. Geophys. Res. Ocean.*, *102*(C1), 893–909, doi:10.1029/96JC02938.

Zweng, M. M., J. R. Reagan, J. I. Antonov, A. V. Mishonov, T. P. Boyer, H. E. Garcia, O. K. Baranova, D. R. Johnson, D. Seidov, and M. M. Bidlle (2013), *World Ocean Atlas 2013, Volume 2: Salinity*.

Appendix A. Error assessment

A common approach for estimating eMLR errors relies on propagation of residuals between regression estimates and measurements. We avoid this approach because unresolved modes of variability are not necessarily a problem for the eMLR method if the impact of the variability on C_T is constant between reoccupations [*Goodkin et al.*, 2011] or adjusted for using a ΔC_{bio} correction. Additionally, our use of multiple combinations of regression parameters revealed that regressions with relatively poor fits to data (e.g. Regression 2, lacking both AOU and *N*) produce ΔC_{anth} estimates that agree within expectations with estimates for regressions with better fits.

Instead, we build our error estimate from a consideration of the likely error sources:

1. measurement errors or errors in our measurement adjustments (see Section 2.1);
2. violations of the eMLR assumption that C_T changes from C_{anth} increases are the only non-stationary mode of variability;
3. the semi-arbitrary choice of regression constant combinations;
4. and other deficiencies inherent on eMLR.

Errors from these sources are estimated independently and combined as the square root of the sum of squared error contributions from these 4 items.

Field Code Changed

Deleted: ΔAOU

Formatted: Font: (Default) Times New Roman, 12 pt

Deleted: <#>violations of the eMLR assumption that C_T changes from C_{anth} increases are the only non-stationary mode of variability;¶

Deleted: ;¶

Formatted: Font: (Default) Times New Roman, 12 pt

Deleted: 3

Formatted: Font: (Default) Times New Roman, 12 pt

Errors from the first two sources are estimated using C_{anth} estimates made with perturbed data. We perturb the later data sets of each data set pair by subtracting offsets that represent either long-term trends or measurement inaccuracies in the properties. For θ, S, C_T, AOU, N, and Si, our perturbations (0.002, 0.002, 2, 2, 0.4, and 0.4 µmol kg^{-1}, respectively) primarily reflect assumed measurement or adjustment uncertainties. For T and S, seasonal cycling and ongoing climate changes are creating greater property differences than measurement inaccuracies are. We therefore scale warming and freshening rate estimates for SAMW and AAIW from [*Böning et al.*, 2008] and for bottom waters from *Purkey and Johnson* [2010; 2013] with depth (z) and the length of time elapsed between occupations (δt), and add them together to obtain an ad hoc estimate of likely T and S changes (Δs):

$$\Delta_T = \left(0.009\frac{600\text{ m}}{z+100\text{m}} + 0.005\min\left(1, \frac{500\text{ m}}{\text{abs}(z-5000\text{ m})}\right)\right)\frac{°\text{C}}{\text{yr}}\delta t \qquad \text{(A1)}$$

$$\Delta_S = \left(0.001\frac{600\text{ m}}{z+100\text{ m}} + 0.0005\min\left(1, \frac{500\text{ m}}{\text{abs}(z-5000\text{ m})}\right)\right)\frac{1}{\text{yr}}\delta t \qquad \text{(A2)}$$

The first terms in parentheses reflect changes in thermocline water masses. The second terms use minimum functions to allow AABW changes to apply uniformly over the 4500 to 5500 m depth range and decrease outside of this range. Figure A1 is an example of the changes that would be assigned T and S from sections repeated 10 years apart. The 6 perturbed data sets are then propagated through our calculations (omitting the deep data difference adjustment) and the differences between the estimates produced with the perturbed and un-perturbed runs are used as error estimates. Differences between the 6 perturbed runs and the unperturbed run create 6 sets of C_{anth} concentration, column inventory, and basin inventory error estimates (e_1 through e_6).

Deleted: two sources

Formatted: Font: Italic

Formatted: Font: Italic

Deleted: of

Formatted: Normal

For column and basin inventory estimates, e_1 and e_2—representing uncertainties in C_T and AOU—are divided by 2 because we are more confident in our dataset adjustments than in individual measurements for these measurements. These perturbations only affect our estimate uncertainties, so errors in our assumed rates of warming and freshening have no impact on our C_{anth} estimates.

Deleted:

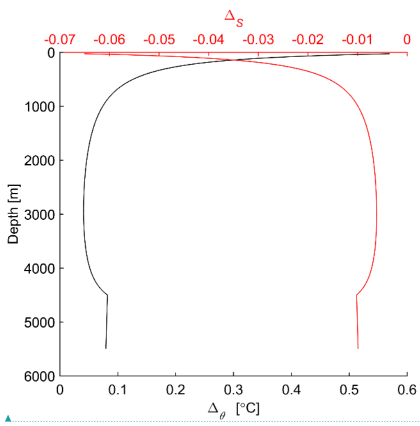

Formatted: Font: (Default) Times New Roman, 12 pt, Italic

Figure A1. Example warming and freshening estimates for temperature (Δ_T, black line, lower X-axis) and salinity (Δ_S, red line, upper X-axis) as a function of depth for data from cruises 10 years apart. Equations for these lines are given in equations (A1) and (A2).

Plancherel et al. [2013] showed eMLR estimates are sensitive to the choice of properties included in the regressions. We estimate the resulting uncertainty as the standard deviation of the population of C_{anth}, column inventory, and basin storage estimates from the 16 regression property combinations (s_{16}). This uncertainty only reflects errors in our estimate of an ideal mean ensemble eMLR estimate and does not reflect limitations inherent on the eMLR or ensemble eMLR method generally. We assume this error is uncorrelated between our 16 regression property combinations and that it therefore becomes a factor of 4 smaller for ensemble eMLR after averaging our 16 sets of results.

We estimate the final source of error attributable to other inadequacies of the eMLR method in Appendix B, where we find a reconstruction error of 0.55±2.6μmol kg^{-1} (mean±r.m.s.e.) for simulated property distributions with no measurement errors. We call this the minimum error, or e_{min}. This e_{min} estimate reflects an unknown contribution from errors from source 2, as these errors also apply to reconstructions of simulated fields with non-stationary modes of variability.

Overall estimate errors (E, Fig. A2) are estimated according to equation A3:

$$E = \sqrt{\sum_{n=1}^{6} e_n^{\ 2} + \left(\frac{s_{16}}{4}\right)^2} \qquad \text{(A3)}$$

We do not include e_{min} in this estimate because the average r.m.s.e. for individual ΔC_{anth} estimates (±3.5 μmol kg^{-1}) obtained from Equation A3 is already larger than the average estimate we obtain from an independent approach to estimating overall r.m.s.e (±2.7 μmol kg^{-1}) in Appendix B. We therefore contend the majority of e_{min} is accounted for by the perturbation analysis. In our figures estimates are considered significant in figures if they exceed 1.96 times the E specific to that estimate.

Deleted: We

Deleted: , so this error

Field Code Changed

Field Code Changed

Deleted: is

Field Code Changed

Formatted: Not Superscript/ Subscript

Field Code Changed

Deleted: E

Deleted: estimate

Extrapolation errors are potentially large for basin averages estimated from only a pair of hydrographic lines. Lateral tracer gradients resulting from gyre interior circulation pose an additional challenge for extrapolations from P16. However, a reconstruction of our estimates along P02 using the P16 section estimates had a RMSE of only 1 µmol kg^{-1} for both decades, and a 4% and 13% average error in the early and later decades respectively. Given these estimates and the ~20% *E* estimate from Equation A3, we assign our basin inventory change estimates uncertainties of 25% of the total value.

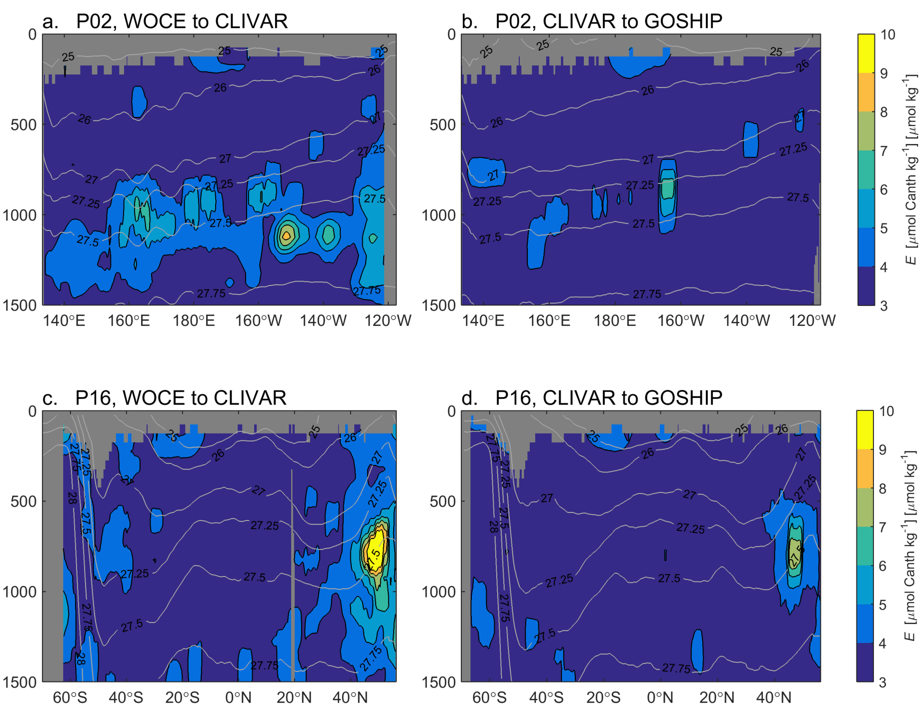

Figure A2. Sections of regionally varying overall uncertainty estimates *E*. Panels are for **a.** P02 in the earlier decade, **b.** P02 in the recent decade, **c.** P16 in the earlier decade, and **d.** P16 in the recent decade. Grey lines are isoneutral surfaces of the labeled γ^N.

Appendix B. Assessing the efficacy of moving windows and ensemble eMLR modifications

We test the efficacy of the ΔC_{bio} (step 2), moving windows (step 4), and ensemble eMLR (step 5) methodological modifications to eMLR for improving C_{anth} storage change estimates using Earth System Model output with known C_{anth} changes. We use a pair of simulations of ocean biogeochemistry with the coupled Earth System Model ESM2M developed at the National Oceanic and Atmospheric Administration's Geophysical Fluid Dynamics Laboratory (NOAA-GFDL). The model consists of a 1° MOM4p1 ocean version [*Griffies et al.*, 2009] coupled to an approximately 2° version of the AM2 atmospheric model [*Anderson et al.*, 2004]. Ocean biogeochemistry is modeled with version 2 of the Tracers of Ocean Plankton with Allometric Zooplankton (TOPAZ2) biogeochemical model [*Dunne et al.*, 2013].

Formatted: Subscript

We consider a perturbation study focusing on the behavior of the TOAPZ2 model in ESM2M that was first presented by *Carter et al.* [2016b]. This specific perturbation study meets our scientific needs as it is based on a concentration-pathway configuration of the model, and allows for a simple definition of C_{anth}. The model was spun up under preindustrial atmospheric CO_2 boundary conditions for more than 1000 model years to minimize drift. Subsequent to the spin-up, the model was run for an additional 70 years with preindustrial boundary conditions for CO_2 as seen by the atmospheric radiation code. Over this same 70 year interval, two instances of the full TOPAZ2 biogeochemical model were run concurrently online. The first instance of TOPAZ2 maintained a constant preindustrial CO_2 boundary condition, while the second imposed a 1% year^{-1} increase in the atmospheric boundary condition for CO_2, such that it achieved doubling after approximately 70 years. As such, the difference in the carbon state variables as

Deleted: [

Deleted: ,

they evolve at each time step between the two TOPAZ2 instances of the 70 year period serves as our definition of C_{anth}. With identical ocean circulation, the C_T disparity that evolves over these 70 years is thereby attributable to C_{anth} storage. We use ensemble eMLR to reconstruct these C_T changes from model year 1995 to 2005 along 5 meridional sections from 90°S to 60°N along 179.5°E, 79.5°E, 59.5°E, 24.5°W, and 95.5°W between 150 and 1000 m depth. We then determine the mean and r.m.s. errors along each section. Finally, we average the absolute values of these errors. We repeat this test with and without latitudinal restrictions on the moving windows, depth/density restrictions on the moving windows, and ensemble averaging.

Table B1. Standard deviations of normally distributed populations of offsets applied to simulated measurements.

Offset	Error type represented	θ	S	C_T	AOU	N	Si
	Units	°C		μmol kg^{-1}	μmol kg^{-1}	μmol kg^{-1}	μmol kg^{-1}
1	Imprecision	0.002	0.002	2	2	0.1	0.1
2	Inaccuracies or shifts	0.01	0.01	1	1	0.4	0.4

A second set of tests is conducted using model outputs that have been perturbed to simulate measurement inaccuracies and imprecisions. We apply two sets of simulated errors to represent these sources of uncertainty. First, we perturb each simulated property value by applying a random offset selected from a normally distributed population with a mean of 0 and a standard deviation equal to the values given in the first row of Table B1 (representing measurement imprecisions). Second, we apply an offset that is identical for all measurements of a given parameter (representing measurement inaccuracy) using standard deviations from the second row in Table B1. The standard deviations for θ and S for this second set of perturbations are large because they also represent potential unresolved un-modeled shifts in the relationships between

Formatted: Font: Italic

Formatted: Font: Italic

Formatted: Subscript

Formatted: Font: Bold

Formatted Table

Formatted: Font: Not Bold, Not Italic, Font color: Auto

Formatted: Space After: 0 pt, Line spacing: single

Formatted: Space After: 0 pt, Line spacing: single

Formatted: Space After: 0 pt, Line spacing: single

Formatted: Space After: 0 pt, Line spacing: single

Formatted: Font: Italic

properties (see Appendix A, error source 2). We repeat this process 20 times for each of our 5 sections, creating a population of 100 realizations of the simulated parameter fields with simulated measurement errors. We then analyze these 100 realizations using traditional and ensemble eMLR and repeat our assessment as before. We also analyze these simulated fields with and without the ΔC_{bio} adjustment in equation (8).

The skill of the technique within these sets of simulations is shown in Table B2. We find the mean error increases by 30-40% when a single regression is used in place of the ensemble mean, while the r.m.s.e. increases nearly twice this amount. Omitting the moving window in latitude leads to a small ~10% improvement in mean error while omitting the moving window in density or depth doubles the mean error (though it is likely the common practice of using multiple regressions for various depth/density ranges works as well as a moving window). Neither window has a strong impact on the r.m.s.e. when the ensemble approach is used. Omitting the ΔC_{bio} adjustment increases the ensemble mean error and the r.m.s.e by ~7-15%. This analysis suggests the overall error with our approach with measurement uncertainties is 1.45±2.7 μmol kg^{-1} (mean±r.m.s.e.), which is smaller than the estimates in Appendix A, and likely represents a best case scenario with little mesoscale variability and an even measurement grid. Except when noted, errors in presented in this manuscript are the errors estimated in Appendix A.

Table B2. Mean error ± r.m.s.e.) in μmol kg^{-1} for eMLR reconstructions of C_{anth} changes in seawater deeper than 150 m depth between 1995 and 2005 along 5 meridional transects in the ESM2M. Columns correspond to analyses done with and without ensemble averaging.

	Ensemble	Non-ensemble
No modifications	0.55±2.6	0.73±4.6
∞ Lat. window	0.60±2.7	1.31±5.3

Formatted: Font: Not Italic

Formatted: Font: Not Italic

Formatted: Subscript

Formatted: Font: Bold

Formatted Table

Formatted: Subscript

Formatted: Space After: 0 pt, Line spacing: single

Formatted: Space After: 0 pt, Line spacing: single

Formatted: Space After: 0 pt, Line spacing: single

∞ depth/density window	1.10±2.5	1.50±4.6
+ simulated errors	1.45±2.7	2.02±4.4
+ simulated errors, no ΔC_{bio}	1.67±2.9	2.50±4.8

OA-related biogeochemical C_T redistribution slightly complicates our use of simulated C_T changes as a ΔC_{anth} benchmark because it is a process affecting C_T distributions other than C_{anth} storage [*Carter et al.*, 2016b]. This redistribution may or may not be removed by subtracting regression coefficients during eMLR. Nevertheless, these changes are at most a small portion of the overall C_T changes: using the ΔAlk* metric of *Carter et al.* [2016b] to quantify the impact of these changes reveals 0.08±0.4 μmol kg^{-1} A_T (mean±r.m.s.e.) change can be attributed to these feedbacks over our study area. This small A_T redistribution would result in an even smaller C_T redistribution from solubility changes or changed activity of the hard tissue pump.

Formatted: Space After: 0 pt, Line spacing: single

Formatted: Font: Not Bold, Not Italic, Font color: Auto, Subscript

Formatted: Space Before: 0 pt, Line spacing: single

Formatted: Font: Italic

Formatted: Subscript

Formatted: Font: Italic

Formatted: Subscript

Formatted: Font: Italic

Formatted: Subscript

Deleted: [

Deleted: ,

Formatted: Font: Italic

Formatted: Subscript

Formatted: Font: Italic

Formatted: Subscript

Formatted: Font: Italic

Formatted: Subscript

Page 14: [1] Change	Unknown	

Field Code Changed

Page 14: [2] Deleted	Brendan Carter	9/30/16 5:08:00 PM

are used

Page 14: [2] Deleted	Brendan Carter	9/30/16 5:08:00 PM

are used

Page 14: [3] Change	Unknown	

Field Code Changed

Page 14: [4] Deleted	Brendan Carter	9/30/16 5:14:00 PM

Regressions with AOU always return a ΔAOU equaling 0. Example Equations (3) and (4) correspond to Reg. # 3 in this table.

Page 14: [5] Change	Unknown	

Field Code Changed

Page 14: [6] Change	Unknown	

Field Code Changed

Page 14: [7] Change	Unknown	

Field Code Changed

Page 14: [8] Change	Unknown	

Field Code Changed

Page 14: [9] Change	Unknown	

Field Code Changed